Dear Dr Folch,
We thank you a lot for your valuable comments and suggestions. We addressed them as explained below.
The reviewer's comments are repeated in **bold letters**, our replies are given in standard font, and text modified or added to the manuscript is given in blue.

This paper uses the ICON-ART modelling system to study the effects of volcanic aerosol dynamics (alterations in aerosol size and composition due to particle aging) and aerosol-radiation feedbacks on the dynamics of volcanic clouds. It is known that the strong absorption of fine ash particles can cause thermal disequilibrium with the surrounding atmosphere, potentially altering the atmospheric dynamics. However, in-depth studies are scarce in the literature and this paper is an important step forward. The authors show results for the 2019 Raikoke eruption, using measurements from different satellite instrumentation for model validation; TROPOMI and AHI for SO2/ash column mass retrievals, and MOIS/VIIRS/CALIOP/OMPS-LP for cloud top height. It is difficult to extract conclusions from a single example but, overall, I think this paper is very relevant to show the potential effects of both phenomena on model forecasts. I do recommend publication with minor revisions detailed below.

Thank you very much for the insightful review. Your comments and questions helped us a lot to improve the manuscript.

1. ICON-ART is run for 3 scenarios: AERODYN_rad (aerosol dynamics + radiation), no_AERODYN_rad (no dynamics) and AERODYN_no_rad (no radiation), which allow isolating the effects of dynamics and radiation. These are actually in competition, with dynamics enhancing premature settling and radiation uplifting the cloud (as nicely shown in Figure 8). To what extent can these two effects counterbalance? This is somehow discussed in Sec 3.3., but it would be great to compare AERODYN-rad results with the no_AERODYN_no_rad ICON case. Note also that, to my knowledge, all operational volcanic cloud forecast systems do not include neither dynamics nor radiation and therefore the no_AERODYN_no_rad (not shown) would actually mimic current setups.

We agree that operational volcanic cloud forecast centers do neither include dynamics nor radiation interaction. Therefore, a comparison with this simulation case would indeed be beneficial. As we ran ICON-ART in the setup no_AERODYN-no_rad, we add some of these results to the manuscript.

Updated Table 2:
We include the no_AERODYN-no_rad scenario in Table 2.

We add to l. 279:
The fourth scenario represents the status quo of operational volcanic cloud forecast. It considers neither aerosol dynamic effects nor aerosol-radiation interaction.

Updated Fig. 4:
We replace the AERODYN-no_rad by the no_AERODYN-no_rad scenario. For details, please refer to answer of comment 2.

Updated Fig. 6:
We include the two no_rad simulation scenarios in Fig. 6. Furthermore, additional dates with a comparison between CALIOP and ICON-ART model results are displayed in the Appendix of the manuscript.
We add to l. 358:
A similar conclusion can be derived from the AERODYN-no_rad and no_AERODYN-no_rad scenarios in Fig. 6 (e) and (f), respectively. Although, both are missing the most prominent feature between 49° N and 51° N at around 16 km, they show the same behavior in terms of aerosol dynamic effects.
Additional dates of CALIPSO measurements are displayed in Appendix A.

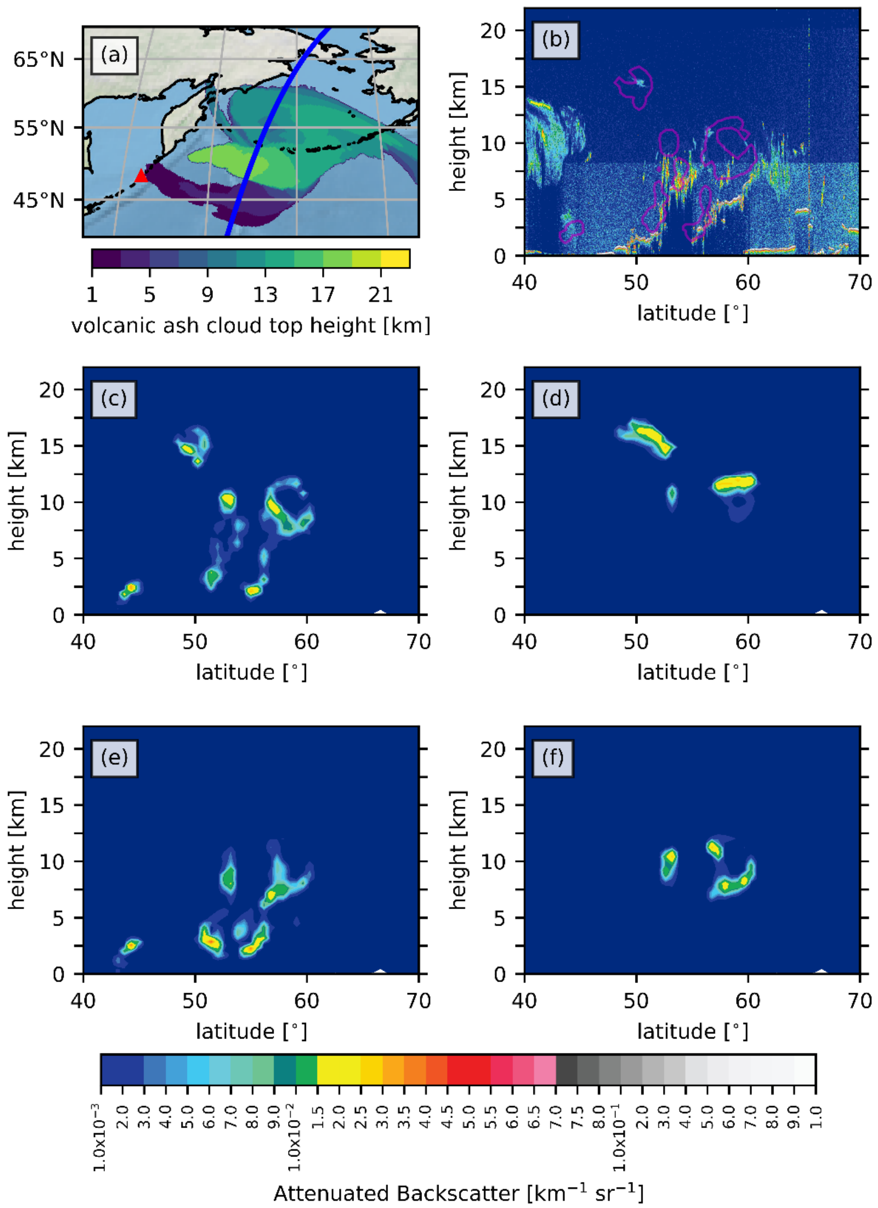

Figure 6. (a) CALIPSO ground track on 23 June 2019, around 15:00 UTC in blue color and location of Raikoke volcano as red triangle. The contour map shows the volcanic ash cloud top height for the AERODYN-rad scenario. (b) The CALIOP attenuated backscatter for 532 nm for the satellite position between 40° N and 70° N is displayed in the top right panel. The magenta line shows the 0.002 km^{-1}sr^{-1} contour of AERODYN-rad at 15:00 UTC. Middle and lower panels: Total attenuated backscatter for 532 nm of volcanic aerosols under the CALIPSO ground track on 23 June 2019, for the 15:00 UTC model output are displayed. (c) shows the result for AERODYN-rad, (d) for no_AERODYN-rad, (e) for AERODYN-no_rad, and (f) for no_AERODYN-no_rad, respectively.

Updated Fig. 8:
We include the no_AERODYN-no_rad scenario plume top height in Fig. 8. Furthermore, we add an error bar for the OMPS measurement in the same figure (as requested by referee #1).
For further explanation we rephrase l. 410:
A distinct difference prevails between the two scenarios with radiative interaction (yellow and green curve) and the two without radiative interaction (pink and orange curve).

And add to l. 420:
As for accumulation mode particles, in the no_AERODYN-no_rad scenario (orange curve) coarse mode particles also tend to stay on the same height level.

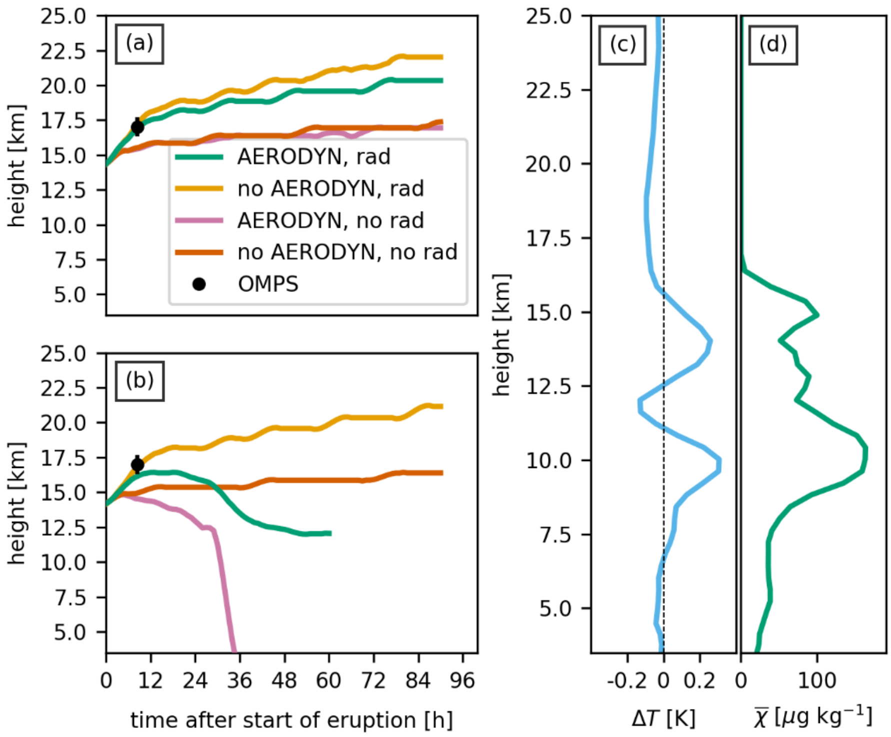

Figure 8. (a) and (b) Evolution of height of volcanic ash cloud top after the onset of the eruption on 21 June 2019, at 18:00 UTC. The yellow curve represents the no_AERODYN-rad scenario, the green curve AERODYN-rad, the pink one AERODYN-no_rad, and the orange one represents the no_AERODYN-no_rad scenario. Panel (a) shows the ash cloud top of particles in the accumulation mode, (b) of particles in the coarse mode, respectively. The black circle depicts the volcanic cloud top height obtained from OMPS-LP. (c) Mean temperature difference (AERODYN-rad – AERODYN-no_rad) in volcanic ash cloud columns on 23 June 2019, 12:00 UTC. (d) Mean volcanic ash concentration $\bar{\chi}$ for the same model columns as in (c) for AERODYN-rad.

2. Figure 4 is very interesting but panels (c)-(e) (and (d)-(f)) are difficult to distinguish and should highlight differences better (e.g. using a log scale). A better option could be plotting relative differences (in percent) between both model configurations, using AERODYN_rad as the "true". Is it a 10\% or a 100\%? Difficult to say from (d)-(f) with the contour range used.

We updated Fig. 4 in two ways. First of all, we replaced panels (e) and (f) by the total column ash mass loading of the no_AERODYN-no_rad case. Secondly, we added panels (g) and (h) which are showing the absolute difference between the two simulation scenarios AERODYN-rad – no_AERODYN-no_rad.

We add to and rephrase l. 293:
These differences are mainly restricted to the slightly higher mass loading in panel (e) and small differences in the volcanic cloud structure. For the first day after the eruption, the aerosol dynamic effects and the aerosol-radiation interaction have only a minor influence on the volcanic ash mass loading.
We add to and rephrase l. 300ff.:
Compared to these two simulations, the averaged AHI measurements (Fig. 4 (b)) show values for the maximum ash mass loading that lie in between the two simulation scenarios. In panels (g) and (h) the differences between the two are highlighted by the absolute difference of AERODYN-rad – no_AERODYN-no_rad. It shows that considering aerosol dynamics and aerosol-radiation interaction results in lower volcanic ash mass loadings in most parts of the volcanic cloud. Only for the first day after the eruption, the volcanic cloud seems to be shifted slightly north in the AERODYN-rad scenario compared to the no_AERODYN-no_rad scenario, as the difference plot shows some positive values between 160 – 170° N.

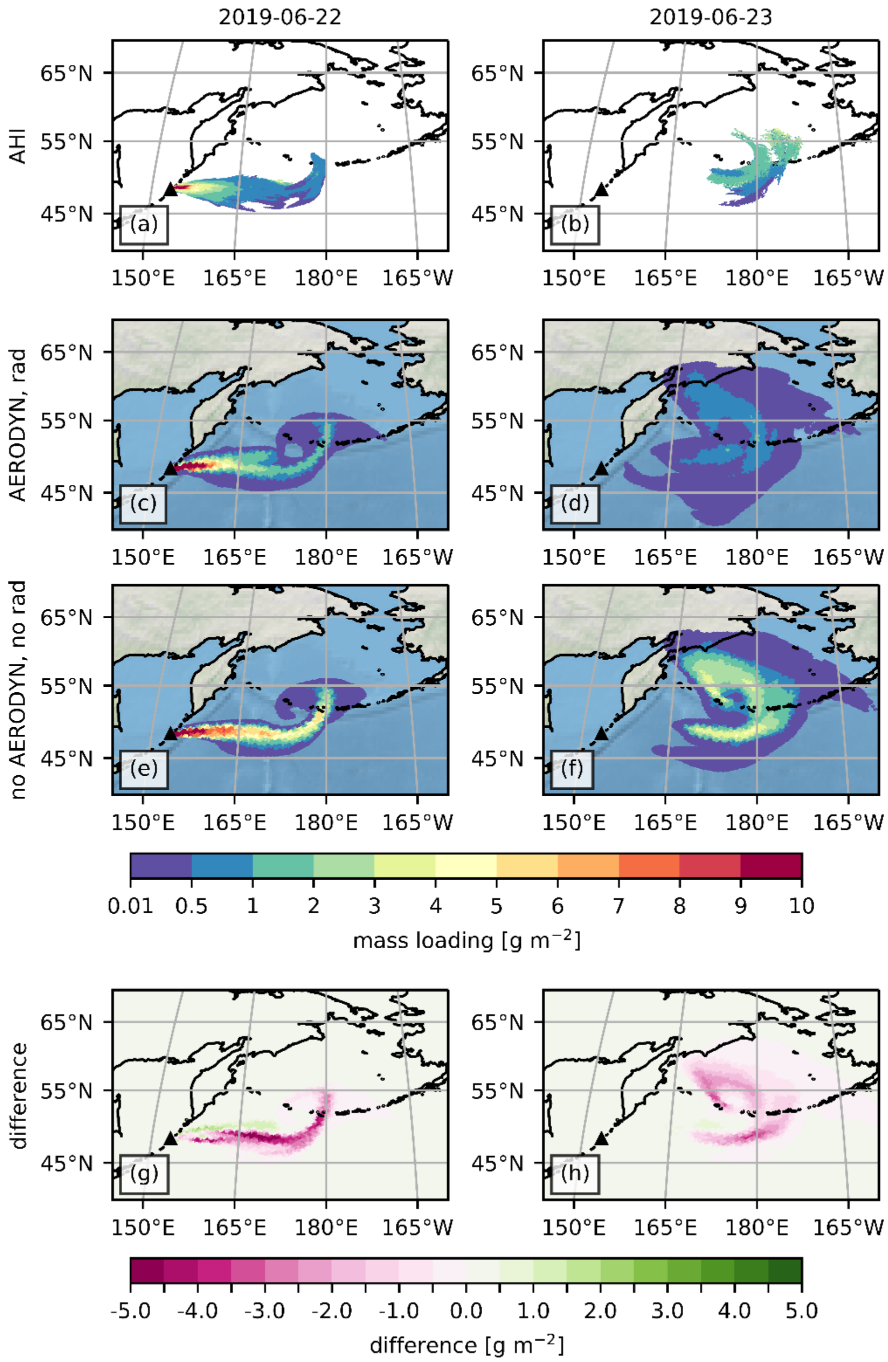

Figure 4. Daily mean total column mass loading of volcanic ash on 22 June (left column) and 23 June 2019 (right column). Top row (panel (a) and (b)) shows results measured by AHI on-board Himawari-8. The middle and lower row (panel (c) - (f)) show ICON-ART results for AERODYN-rad and no_AERODYN-no_rad, respectively. The black triangle depicts the location of Raikoke volcano. Panels (g) and (h) show the absolute difference between the two simulation scenarios.

3. On the other hand, and related to the point above, I missed some figure or text showing the impact on the atmospheric dynamics when switching on the AERODYN_rad module. To what extent is the vertical wind field advecting the cloud modified by thermal perturbations? Can you quantify? I understand that this question may fall beyond the objective of the paper, but it could be of interest to the volcanic cloud modelling community. Ensemble forecast strategies are gaining more and more attention, and these rely on perturbing uncertain variables like the eruption source parameters or the wind field (but rarely the vertical component). As a result, an interesting question it to assess whether (vertical) wind perturbations caused by radiation feedbacks are comparable to typical uncertainties in NWP models. If in the range, an ensemble of offline models could still capture this effect, at least to some extent.

If we look at the most pronounced lifting of the volcanic cloud top height (approx. 3 km, compare Fig. 8) during the first 12 h of the simulation, we obtain an average vertical lifting velocity of 0.07 m/s. This lifting is only visible for simulation scenarios with radiation interaction.
We determined the vertical velocity difference between the AERODYN-rad and the no_AERODYN-no_rad scenario as well as between the AERODYN-rad and AERODYN-no_rad scenario. Both comparisons show comparable numbers. For the comparison, we only consider grid cells which are within a vertical column which contains a volcanic ash mass loading > 0.01 g m^{-2}. The maximum absolute difference that appears locally during the first 12 h of the eruption is in the order of 0.19 m/s with a 98th percentile of 0.05 m/s. We would like to note, that these vertical velocity perturbations strongly depend on the spatial resolution. For a finer resolution, locally we would expect higher vertical velocities.

We include this information in the manuscript in l. 431ff.:
The resulting vertical velocity perturbation Δw is in the order of 0.1 m s^{-1}. For this purpose, we analyzed the difference in vertical velocity between the AERODYN-rad and AERODYN-no_rad scenario during the first 12 h after the eruption. Only grid cells in model columns which contain a volcanic ash mass loading > 0.01 g m^{-2} in both scenarios are considered. Locally, Δw reaches 0.19 m s^{-1} with a 98th percentile of 0.05 m s^{-1}. This agrees well with the vertical lifting of the volcanic cloud top height of around 3 km during the first 12 h ($\overline{w}$ = 0.07 m s^{-1}).

4. The aerosol dynamics module (ARODYN) has pre-defined initial aerosol size distributions, which (if I am not wrong) are evolved according to prognostic equations. How does the aging mechanism depend on this initial condition? Particle distributions can vary notably from one eruption to another, and a single representation could be misleading.

We agree that particle size distributions (PSDs) can vary notably from one eruption to another. For the Raikoke simulation, we defined the emitted PSD as specified in Table 1 in the manuscript. This emitted PSD changes over time as particles age and sediment.
Very often, there is lack of direct measurements when it comes to the PSD of volcanic ash from one particular volcanic eruption like Raikoke. To overcome this limitation, we used the PSD data from five eruptions (listed in the following table) to calculate a generic PSD for volcanic ash in ICON-ART (shown in the following figure). This PSD captures the variability of fine and coarse particles. We are aware of the uncertainties associated with

this generic PSD. Nevertheless, even direct measurements are subjected to large uncertainties and might fail to represent the variability of the PSD.
The aging mechanism which is implemented in AERODYN depends on the PSD. As condensation of gaseous species on existing particles, coagulation, sedimentation, and deposition directly depend on the particle diameter. However, it needs further studies in order to quantify how the aging mechanism depends on the emitted size distribution.

Table: Volcanic eruption for which validated ash PSD data exist (from http://www.ct.ingv.it/iavcei/results.htm)

Eruption	**Montserrat (West Indies)** **31 March 1997**	**Mt. St. Helens (USA)** **18 May 1980**	**Ruapehu (New Zealand)** **17 June 1996**	**Spurr (Alaska)** **16-17 September 1992**	**Eyjafjallajökull (Iceland)** **14 April-21 May 2010** **(data for 4-8 May 2010)**
Eruption type	dome collapse (co-PF plumes)	Plinian+coignimbrite (strong plume)	sub-plinian (weak plume)	sub-plinian	long-lasting weak plume

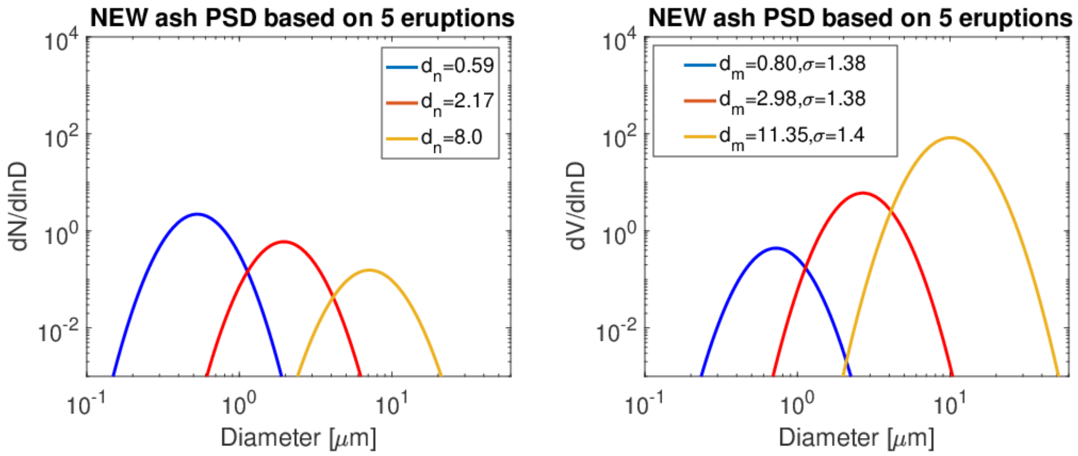

Figure: Calculated ash PSD based on the data available in literature

Bonadonna, C. and Scollo, S.: IAVCEI Commission on Tephra Hazard Modelling, http://www.ct.ingv.it/iavcei/results.htm, last access: 03 September 2020, 2013.

We add to l. 273:
They are based on data from Bonadonna and Scollo (2013).

5. Model validation. Several plots compare model results with observations. However, I missed some quantitative metric values; e.g. SAL, Figure Merit of Space or others. These are by far more objective than color plots (e.g. Figs 4, 5), which can trick depending on the scale and color binning. Given that a main objective of the paper is to "assess if representations of aerosol dynamics and aerosol-radiation interactions are beneficial for forecasts", quantitative metrics would help asking this question more objectively.

We apply the SAL method following Wernli et al. (2008) in order to compare the total column volcanic ash mass loading AHI retrieval with our model result.

Wernli, H., M. Paulat, M. Hagen, and C. Frei, 2008: SAL—A Novel Quality Measure for the Verification of Quantitative Precipitation Forecasts. Mon. Wea. Rev., 136, 4470–4487, https://doi.org/10.1175/2008MWR2415.1

Wernli, H., C. Hofmann, and M. Zimmer, 2009: Spatial Forecast Verification Methods Intercomparison Project: Application of the SAL Technique. Wea. Forecasting, 24, 1472–1484, https://doi.org/10.1175/2009WAF2222271.1

We add the following paragraph to the manuscript in l. 302ff.:
In order to compare our ICON-ART results in an objective manner with the AHI observations, we make use of the SAL method. This quality measure has been introduced by Wernli et al. (2008) and has been extensively discussed by Wernli et al. (2009). The method identifies objects in a 2D field (e.g., total ash mass loading) and quantifies the differences between model and observation in structure (S), amplitude (A), and location (L). A value of 0 implies perfect agreement. We apply the SAL method with a fix threshold value to identify objects R* = 0.01 g m^{-2}. The results for the comparison of daily mean total column mass loading between the AHI retrieval and the ICON-ART results are summarized in Table 3.
The location of the volcanic cloud agrees very well with the observation for all dates in all simulation scenarios. The structure of the volcanic cloud shows larger differences compared to observations, especially on 23 June. However, the values are rather similar for the different simulation scenarios. Only the amplitude values differ distinctly among the different scenarios. Simulations with AERODYN are closer to the observation than simulations without aerosol dynamics.

Table 3: Comparison of daily mean total column mass loading of volcanic ash between AHI and ICON-ART results using the SAL method by Wernli et al. (2008).

	2019-06-22			2019-06-23		
scenario	S	A	L	S	A	L
AERODYN-rad	−0.191	0.584	0.004	1.651	0.298	0.041
AERODYN-no_rad	−0.323	0.579	0.002	1.362	0.275	0.028
no_AERODYN-rad	−0.202	0.921	0.014	1.601	0.716	0.031
no_AERODYN-no_rad	−0.270	0.874	0.013	1.546	0.748	0.030

6. Line 84. "density values less"?

We agree that this formulation is a bit misleading and hope that the reformulation makes it easier to understand.
We change the sentence on p.3 l.84 from:
Only data with the quality descriptor 'qa_value' larger than 0.5 and total vertical column density values less than 1000 mol m^{-2} were used.

to:
Only data with a quality value larger than 0.5 (as recommended in the TROPOMI product user manual) and total vertical column density with values less than 1000 mol m^{-2} were used.

7. Line 257. It is stated that the source term in ICON-ART is set between 8 and 14 km a.s.l. Does it mean a 6 km thick cloud? This seems quite inconsistent with the TROPOMI retrievals, which assume 1 km thickness at 15 km a.s.l.

Yes, in the model simulation we emit a 6km thick cloud of ash and SO_2. Our emission parametrization for ash and SO_2 is based on satellite observations (as well as results of Plumeria and FPlume). The configuration of the emission height has been done specifically for the Raikoke eruption in 2019 and is based on satellite observations and volcanic monitoring reports (Sennet, 2019).
Whereas, the TROPOMI retrieval assumptions have been set for a much broader range of scenarios. The retrieval algorithm can be run with one of four different assumptions on where the SO_2 is located in the atmosphere. This could either be a vertical profile modeled by the global chemistry transport model TM5 or a 1 km thick box in either 1 km, 7 km or 15 km. Comparisons with other satellite products showed, that the assumption of a 1 km box in 15 km a.s.l. gave best results, although, the retrieval assumption does not match with the actual SO_2 distribution in the atmosphere after the Raikoke eruption.

Dear Referee 1,
We thank you a lot for your valuable comments and suggestions. We addressed them as explained below.
The reviewer's comments are repeated in **bold letters**, our replies are given in standard font, and text modified or added to the manuscript is given in blue.

In this study, the authors investigate the importance of aerosol dynamics and aerosol-radiation interactions in the early dispersion of the volcanic plume injected by the Raikoke eruption in June 2019. They argue that physical processes influencing the transport of volcanic plumes in the UTLS region have been poorly addressed compared to work related to source parameters/initial conditions. Using a set of satellite observations including HIMAWARI-8, CALIOP and OMPS-LP, they attempt to validate their simulations of the ICON-CART global modelling system. This is a very interesting and unique study that attempt to shed light on how a complex aerosol-dynamic-radiation coupling system can be used to understand early evolution of volcanic plumes and thus is suitable for publication in the Atmospheric Chemistry and Physics Journal. However, I believe that additional work would need to be done to validate the model results. With only one CALIPSO browse image and one OMPS-LP volcanic plume top point, the vertically resolved information that offer a unique opportunity to validate model results are not fully explored. Before this manuscript can be published, I would recommend the authors to provide additional observational evidences to support their conclusions.

Thank you very much for the insightful review. Your comments and questions helped us a lot to improve the manuscript.
We agree that additional observational data, especially in form of OMPS-LP volcanic cloud top height, would be very beneficial for the validation of the model results. Unfortunately, we were not able to retrieve any meaningful volcanic cloud height from OMPS-LP measurements for other dates. The reason for this is discussed in more detail together with the answer to comment 7.
The CALIOP measurements show a signal that can be associated with the volcanic cloud on other dates as well. We included these in our answers to the respective comments.

1. P1L3: I agree with this statement but essential information about mass injection rates and plume injection heights are still critical parameters to simulate volcanic plume dispersion.

Yes, we totally agree with you that the correct representation of source parameters is very critical for a reliable forecast of volcanic aerosols. Especially, estimates about the mass eruption rate and plume height are crucial for short term forecasts right after volcanic eruptions. This is why they are still substance of ongoing research. With this work, we don't intend to diminish the importance of source parameters, but shed light on less studied sink processes.

2. P1L10: I would replace "show" by "suggest" since I'm not certain that the results presented in this paper really fully support the conclusions.

During the review process we had the opportunity to provide further evidence for our statement. This is why we would like to leave it as is.

3. P2L36: I would argue that the rise of the plume is better documented by the two initial papers from Khaykin et al., 2017 and Peterson et al., 2017.

We additionally cite the suggested two papers:

Khaykin, S. M., Godin-Beekmann, S., Keckhut, P., Hauchecorne, A., Jumelet, J., Vernier, J.-P., Bourassa, A., Degenstein, D. A., Rieger, L. A., Bingen, C., Vanhellemont, F., Robert, C., DeLand, M., and Bhartia, P. K.: Variability and evolution of the midlatitude stratospheric aerosol budget from 22 years of ground-based lidar and satellite observations, Atmos. Chem. Phys., 17, 1829–1845, https://doi.org/10.5194/acp-17-1829-2017, 2017.

Peterson, P. K., Pöhler, D., Sihler, H., Zielcke, J., General, S., Frieß, U., Platt, U., Simpson, W. R., Nghiem, S. V., Shepson, P. B., Stirm, B. H., Dhaniyala, S., Wagner, T., Caulton, D. R., Fuentes, J. D., and Pratt, K. A.: Observations of bromine monoxide transport in the Arctic sustained on aerosol particles, Atmos. Chem. Phys., 17, 7567–7579, https://doi.org/10.5194/acp-17-7567-2017, 2017.

We add to the manuscript in l. 31:
This can result in a lofting mechanism of aerosol which is different from the one caused by large scale atmospheric dynamics as described for example by Khaykin et al. (2017).

In l. 34:
Peterson et al. (2017) observed in the Arctic near-surface atmosphere that the transport of atmospheric pollutants is influenced by active halogen chemistry.

4. P3L83: Could you explain what's the implications of selecting qa_value larger than 0.5?

The qa_value is described in the ESA Tropomi User Manual as followed:
"The quality value or qa_value is a continuous quality descriptor, varying between 0 (no data) and 1 (full quality data). Recommend to ignore data with qa_value < 0.5 (static)" (Sentinel-5 precursor/TROPOMI Level 2 Product User Manual Sulphur Dioxide SO2, https://sentinel.esa.int/documents/247904/2474726/Sentinel-5P-Level-2-Product-User-Manual-Sulphur-Dioxide , accessed 23 July 2020)
In order to improve comprehensibility, we reformulate P3L83
Only data with the quality descriptor 'qa_value' larger than 0.5 and total vertical column density values less than 1000 mol m^{-2} were used.

to:
Only data with a quality value larger than 0.5 (as recommended in the TROPOMI product user manual) and total vertical column density with values less than 1000 mol m^{-2} were used.

5. P4L109: One sentence about the adjustment technique could be explained here.

We rephrase and add some extra information in l.109.
Water vapor and clouds cause interference with the SO_2 signal and introduce a positive bias. Therefore, a retrieval scheme was devised to minimize the interfering effects. In short, the bias is minimized by subtracting an offset SO_2 retrieval for a small region where no SO_2 is believed to exist.

6. P5L126: What could be the impact of ice on those estimates?

We thank the reviewer for raising this as it is a very good point and one that we should have addressed in the manuscript. Ice formation in volcanic clouds is a known problem and happens often, especially in water-rich and tropical eruptions where moist air entrainment happens see Prata et al. (2020). Ice has a very clear infrared spectral signature that can be used to diagnose its presence in volcanic clouds. For Raikoke this signature was absent or at best, weak. True-color images from the Himawari-8 satellite also show no obvious signs of ice - the clouds are dark brown and become paler with time, presumably because of dispersion. The absence of an ice signature can be explained by the high altitude of the emissions (>8 km and up to 15 km) which deposited them into a very dry part of the atmosphere, and the lack of a water-rich plume to begin with, as evidenced in the true-color and IR spectral signature data. The presence of ice reduces the ash mass estimates by an amount that depends on the proportion of the pixel covered by ice. Ice formation could have occurred in the early (first few hours of the eruption on 21 June) as the plume ascended through a moister part of the atmosphere. This could partly explain why ash estimates at the start of the eruption are low; but ash opacity is also a factor that reduces the ash mass retrieval.

Prata, A.T., Folch, A., Prata, A.J., Biondi, R., Brenot, H., Cimarelli, C., Corradini, S., Lapierre, J. and Costa, A., 2020. Anak Krakatau triggers volcanic freezer in the upper troposphere. Scientific reports, 10(1), pp.1-13.

In order to address this issue, we add the following to the manuscript at l.120:

The presence of ice reduces the ash mass estimates by an amount that depends on the proportion of the pixel covered by ice. However, during the Raikoke eruption, ice was not observed except possibly at the start of the eruption which could cause lower ash mass estimates.

7. P6L167: This is very unlikely that the Ambae eruption had a significant impact on stratospheric aerosols beyond the tropics and sub-tropics and thus it seems unrealistic to consider that Ambae could impact the retrieval of a fresh volcanic plume within the OMPS data set within the latitude band where the Raikoke was transported during the first few days.

As the study of Malinina et al. (2020, in review at ACP) on the Ambae eruption shows, the Ambae plume spreads up to 40N until the end of 2018, where its influence still remains non-negligible. Thus, influence of the Ambae eruption at 50N in June 2019 might be expected. We agree with the reviewer that these small residual signals do not affect the retrievals in the core of the fresh Raikoke plume. Unfortunately, the sampling of the OMPS-LP instrument is quite sparse and it does not hit the core of the fresh plume on other days than the one analyzed in the paper. During the analyzed period, in the transition regions of the plume the increase of the aerosol extinction measured by OMPS-LP was not that pronounced and thus can be interfered by residual signals from previous events. We change the manuscript to make this clearer.

Malinina, E., Rozanov, A., Niemeier, U., Peglow, S., Arosio, C., Wrana, F., Timmreck, C., von Savigny, C., and Burrows, J. P.: Changes in stratospheric aerosol extinction coefficient after the 2018 Ambae eruption as seen by OMPS-LP and ECHAM5-HAM, Atmos. Chem. Phys. Discuss., https://doi.org/10.5194/acp-2020-749, in review, 2020

We additionally cite Malinina et al. (2020) in l. 161:
Detailed information on the retrieval algorithm can be found in Malinina (2019) and Malinina et al. (2020).

We rephrase l. 165ff.:
In the following days, when the plume started to spread over the North Pacific, the core of the fresh plume is not hit by the OMPS-LP instrument sampling anymore. Slightly perturbed aerosol extinction observed in transition regions has a similar magnitude as that from interfering events, e.g., the aerosol transport from the Ambae eruption that occurred 11 months earlier, and thus cannot be attributed exclusively to the Raikoke eruption. For this reason, we excluded the OMPS-LP measurements in transition regions from the consideration.

8. P9L240: The treatment of externally mixed ash and sulfuric acid would be more accurate through T-Matrix calculation than Mie Theory. I think this could be further discuss in the manuscript since it seems to be an important element.

We agree with the reviewer that T-Matrix calculations are a powerful tool to determine the radiation interaction of non-spherical aerosols, such as volcanic ash. However, in this work in combination with the newly developed AERODYN module, we allow the formation of internally mixed particles, such as volcanic ash coated with a shell of sulfate and water. To our knowledge there is no T-Matrix code that can handle core-shell assumption. That is why we make use of Mie Theory assuming a core-shell mixing state.
Due to the coating, a spherical assumption for these mixed particles might be reasonable. It is only for consistency reasons, why we chose to apply the sphericity assumption also to the uncoated ash particles. Implementing coated non-spherical ash particles into ICON-ART or considering the non-sphericity of uncoated particles together with internally mixed ones remains the subject of future work.

9. P15L349: The other optical properties (depolarization/color ratio/vertical feature mask) from the plumes from CALIPSO are not shown. This would certainly help with the interpretation as well.

We agree that other optical properties retrieved from CALIOP measurements, such as depolarization ratio, give beneficial information about the composition of the aerosol cloud. In the current state of ICON-ART we don't have forward operators for these quantities. However, to our knowledge it is the first model that retrieves the total attenuated backscatter for internally mixed volcanic aerosol. This is why in this paper, we only compare the total attenuated backscatter at 532nm.

In the manuscript we argue that model results could help to interpret observations better. As an example, we took two images of the CALIOP Aerosol Subtype classification of two dates when the satellite passed over the volcanic cloud. In both images the blue rectangle highlights an area where the plume is located in our model result and also shows a signal in the total attenuated backscatter measured by CALIOP. For the first date, the detected aerosol (within the blue box) is classified only partly as volcanic ash. Based on our model result for the same date we would argue, that in fact the here classified dust is volcanic ash as well. For the other image, there is no aerosol type classified within the blue box. However, the total attenuated backscatter clearly shows a signal and our model results suggest that this is indeed volcanic ash.

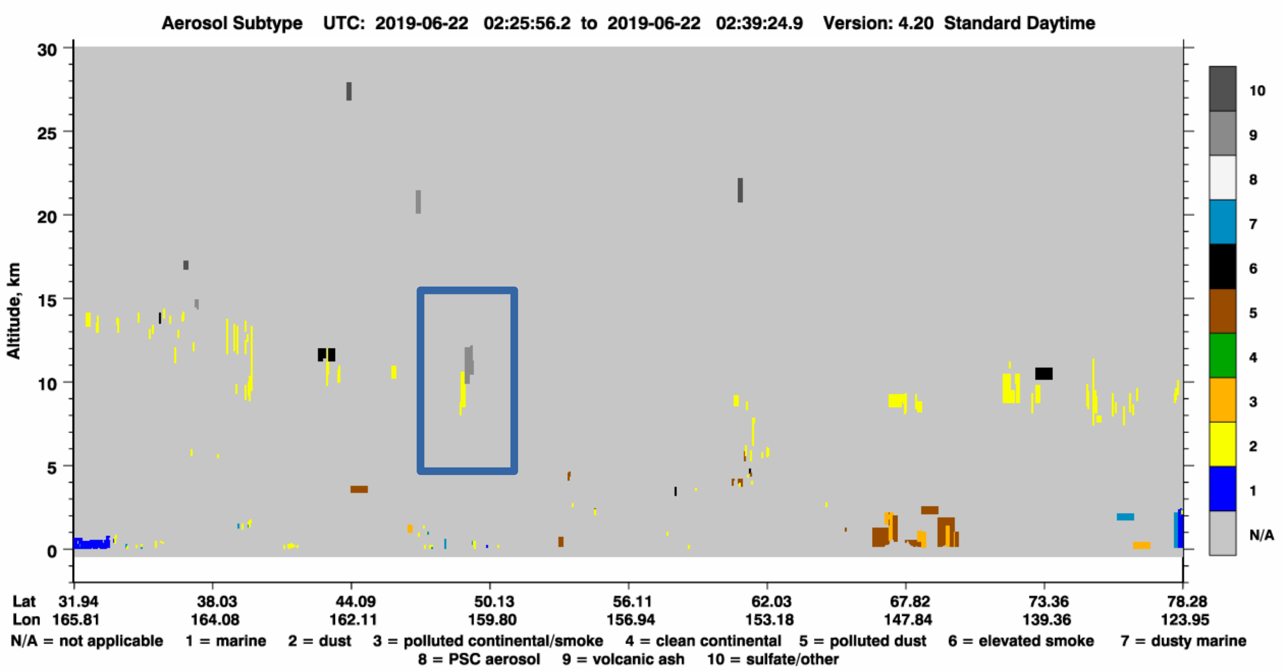

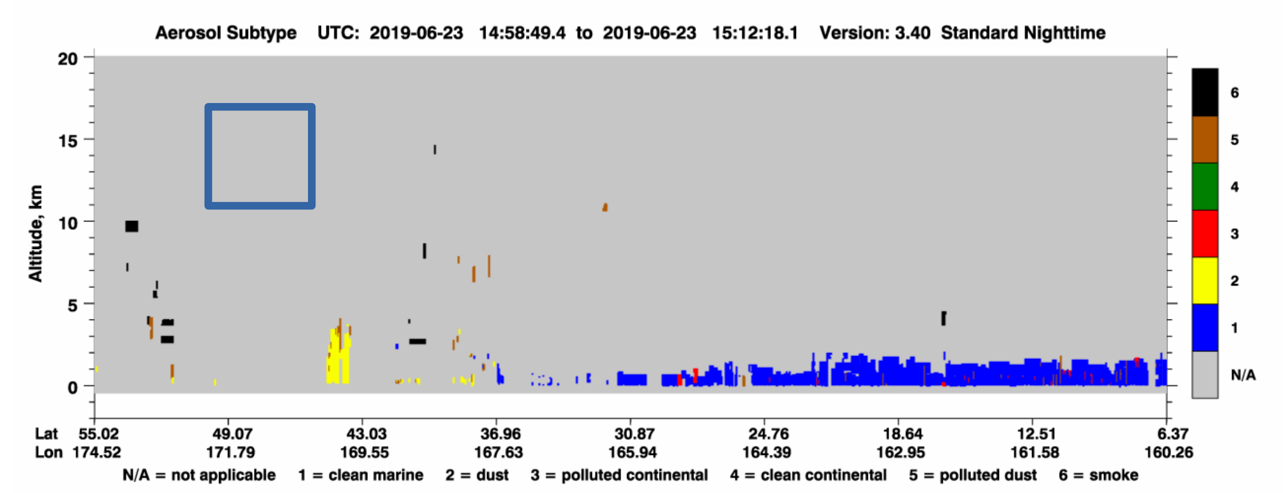

10. Figure 6: Does the model really do a better job representing the volcanic plume with the full dynamical-chemistry-radiation coupling? I'm not really certain that the figure demonstrate that since pieces of plume seen by the AERODYN-rad scenario do not appear clearly on the observations. See link to CALIPSO browse image crossing the volcanic cloud on Jun 22nd for additional obs. that could be used to validate model results. https://www-calipso.larc.nasa.gov/products/lidar/browse_images/show_v4_detail.php?s=production&v=V4-10&browse_date=2019-06-22&orbit_time=01-59-01&page=3&granule_name=CAL_LID_L1-Standard-V4-10.2019-06-22T01-59-01ZD.hdf

We evaluated four additional dates for which CALIPSO passes over the volcanic cloud of the Raikoke 2019 eruption. Furthermore, we extended the model comparison by the two no-rad simulation scenarios as requested by reviewer Arnau Folch. These plots will be displayed in the appendix of the manuscript.

The evaluation of these additional dates confirms our previous statement regarding the improvement of the forecast by including aerosol dynamics and radiation interactions. Only the very last date on June 25 shows no significant improvement.

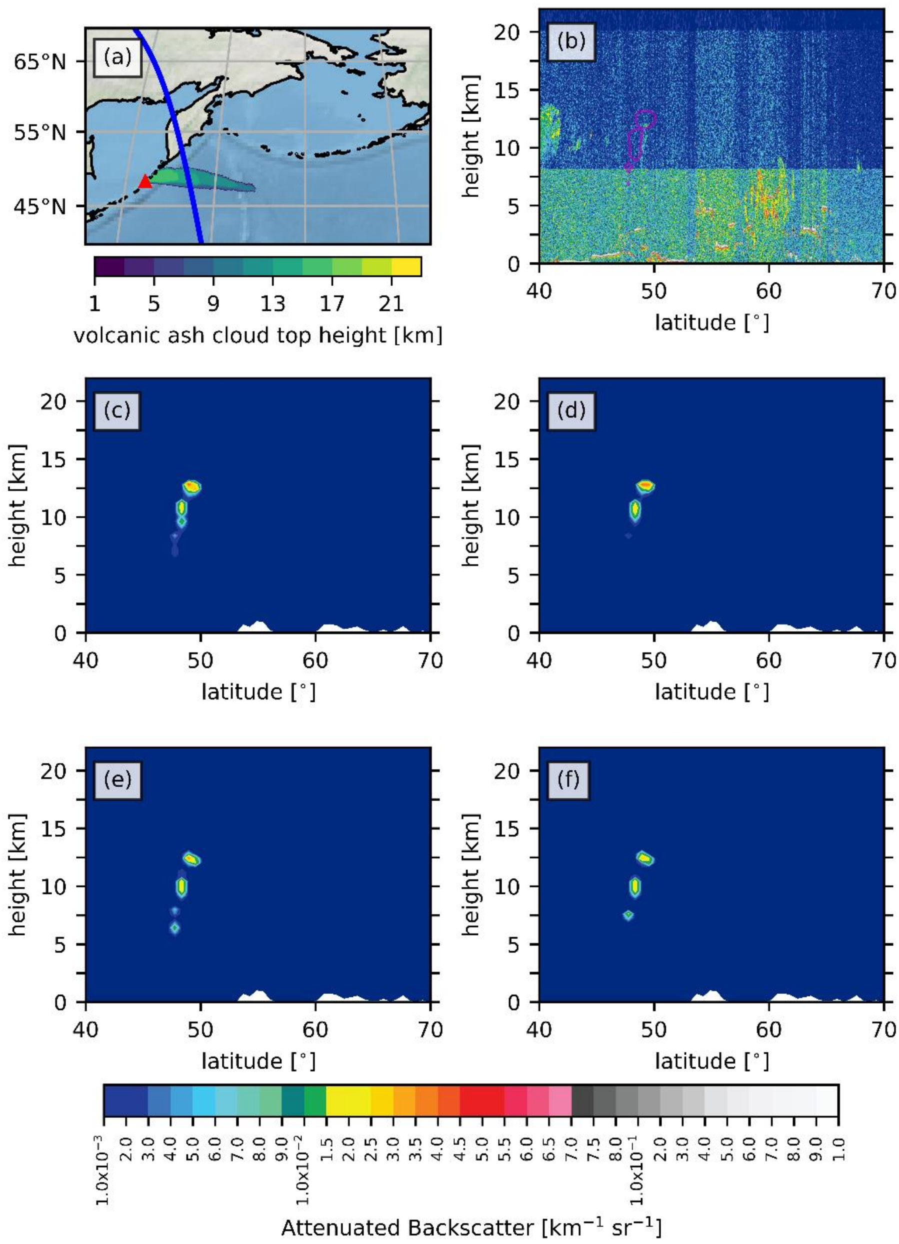

2019-06-22 03:00 UTC
(a) CALIPSO ground track and modeled volcanic cloud top height
(b) Total Attenuated Backscatter at 532 nm measured by CALIOP
(c) AERODYN – rad
(d) no AERODYN – rad
(e) AERODYN – no rad
(f) no AERODYN – no rad

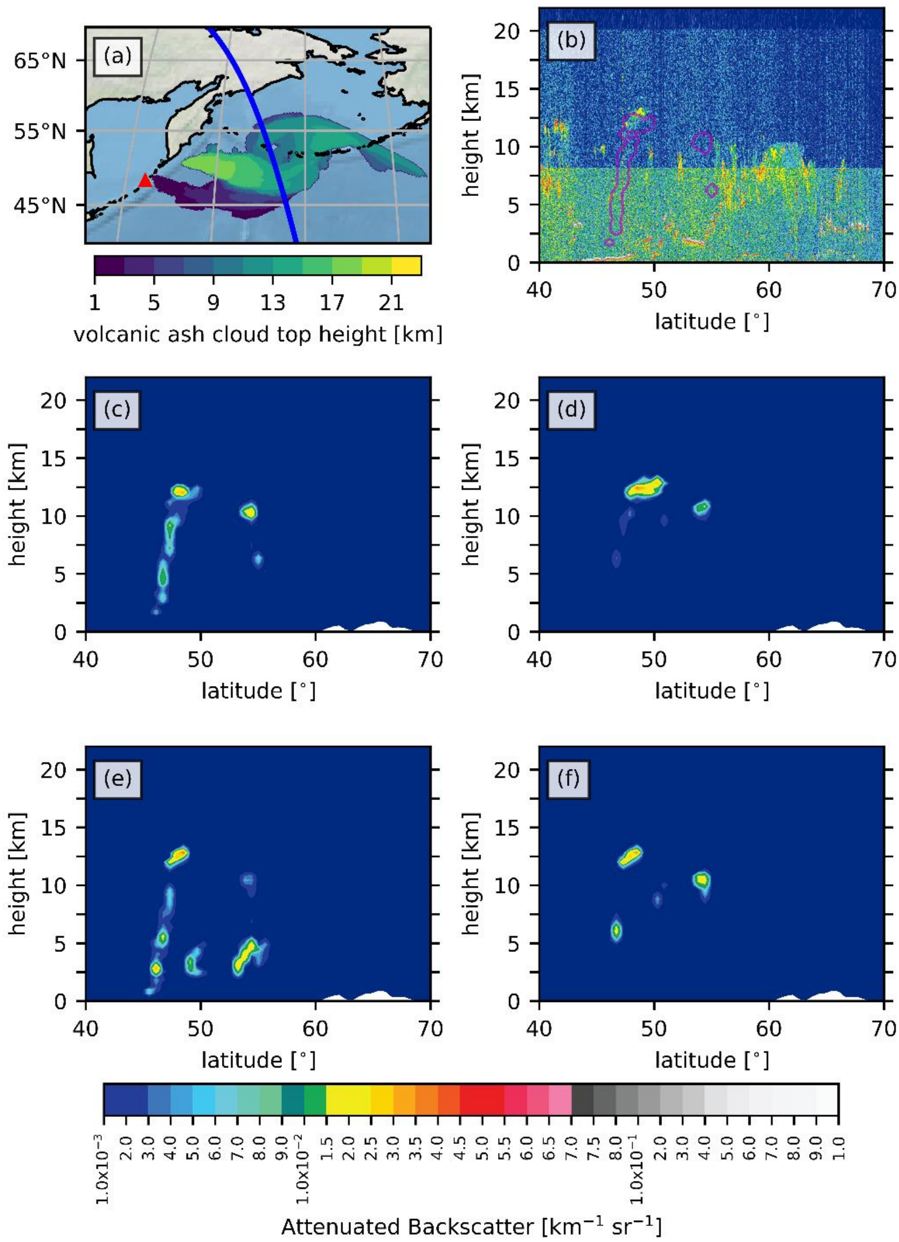

2019-06-23 02:00 UTC
(a) CALIPSO ground track and modeled volcanic cloud top height
(b) Total Attenuated Backscatter at 532 nm measured by CALIOP
(c) AERODYN – rad
(d) no AERODYN – rad
(e) AERODYN – no rad
(f) no AERODYN – no rad

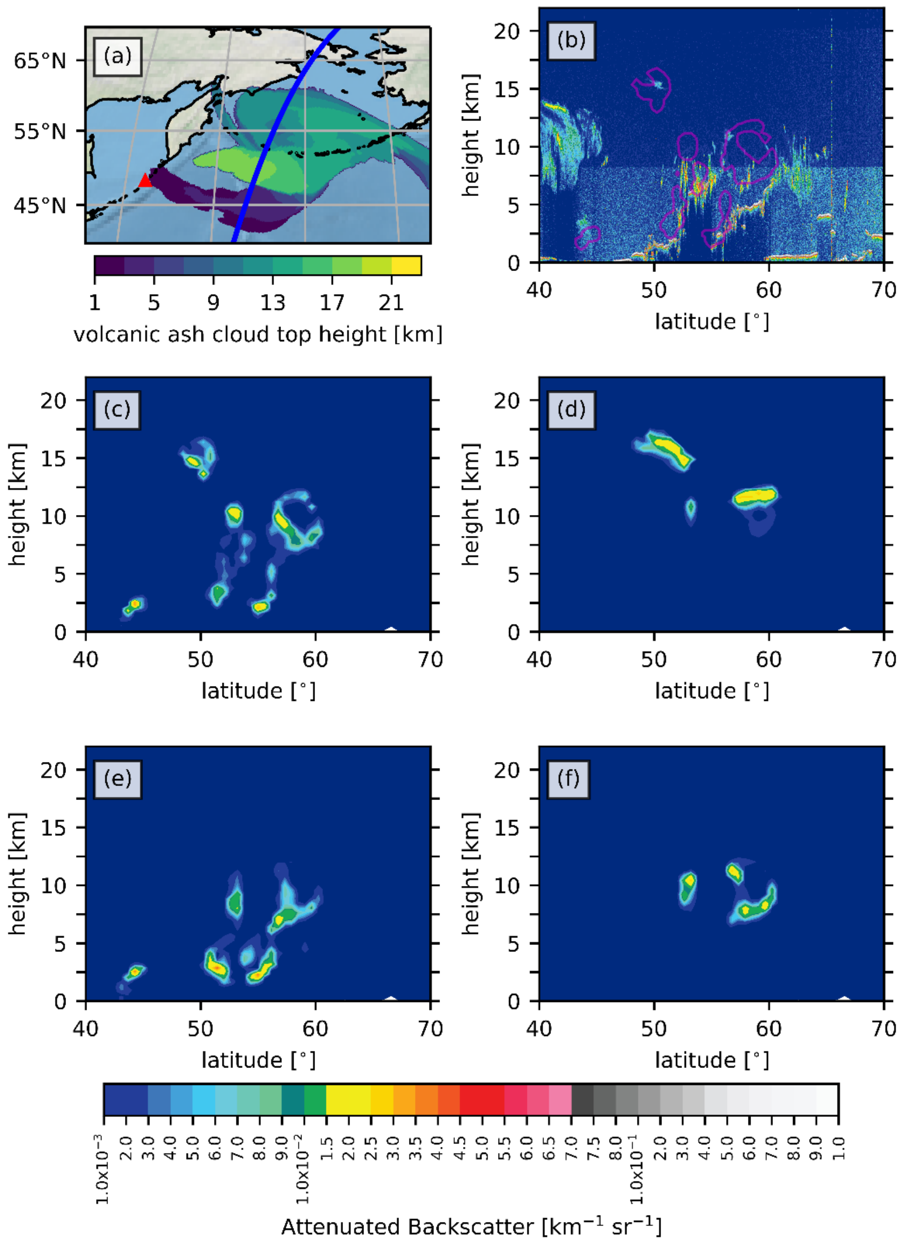

Figure 6. (a) CALIPSO ground track on 23 June 2019, around 15:00 UTC in blue color and location of Raikoke volcano as red triangle. The contour map shows the volcanic ash cloud top height for the AERODYN-rad scenario. (b) The CALIOP attenuated backscatter for 532 nm for the satellite position between 40° N and 70° N is displayed in the top right panel. The magenta line shows the 0.002 km^{-1}sr^{-1} contour of AERODYN-rad at 15:00 UTC. Middle and lower panels: Total attenuated backscatter for 532 nm of volcanic aerosols under the CALIPSO ground track on 23 June 2019, for the 15:00 UTC model output are displayed. (c) shows the result for AERODYN-rad, (d) for no_AERODYN-rad, (e) for AERODYN-no_rad, and (f) for no_AERODYN-no_rad, respectively.

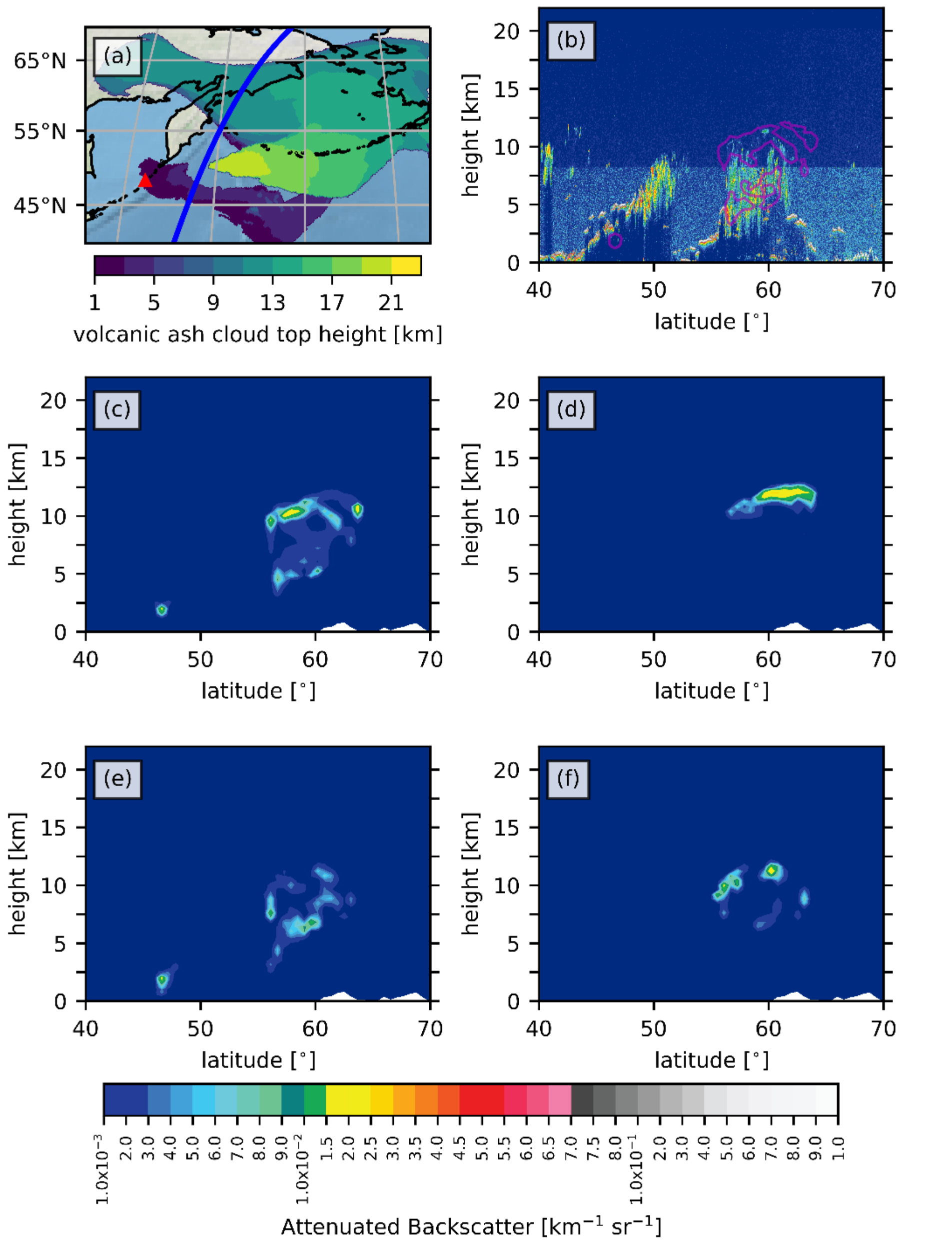

2019-06-24 16:00 UTC
(a) CALIPSO ground track and modeled volcanic cloud top height
(b) Total Attenuated Backscatter at 532 nm measured by CALIOP
(c) AERODYN – rad
(d) no AERODYN – rad
(e) AERODYN – no rad
(f) no AERODYN – no rad

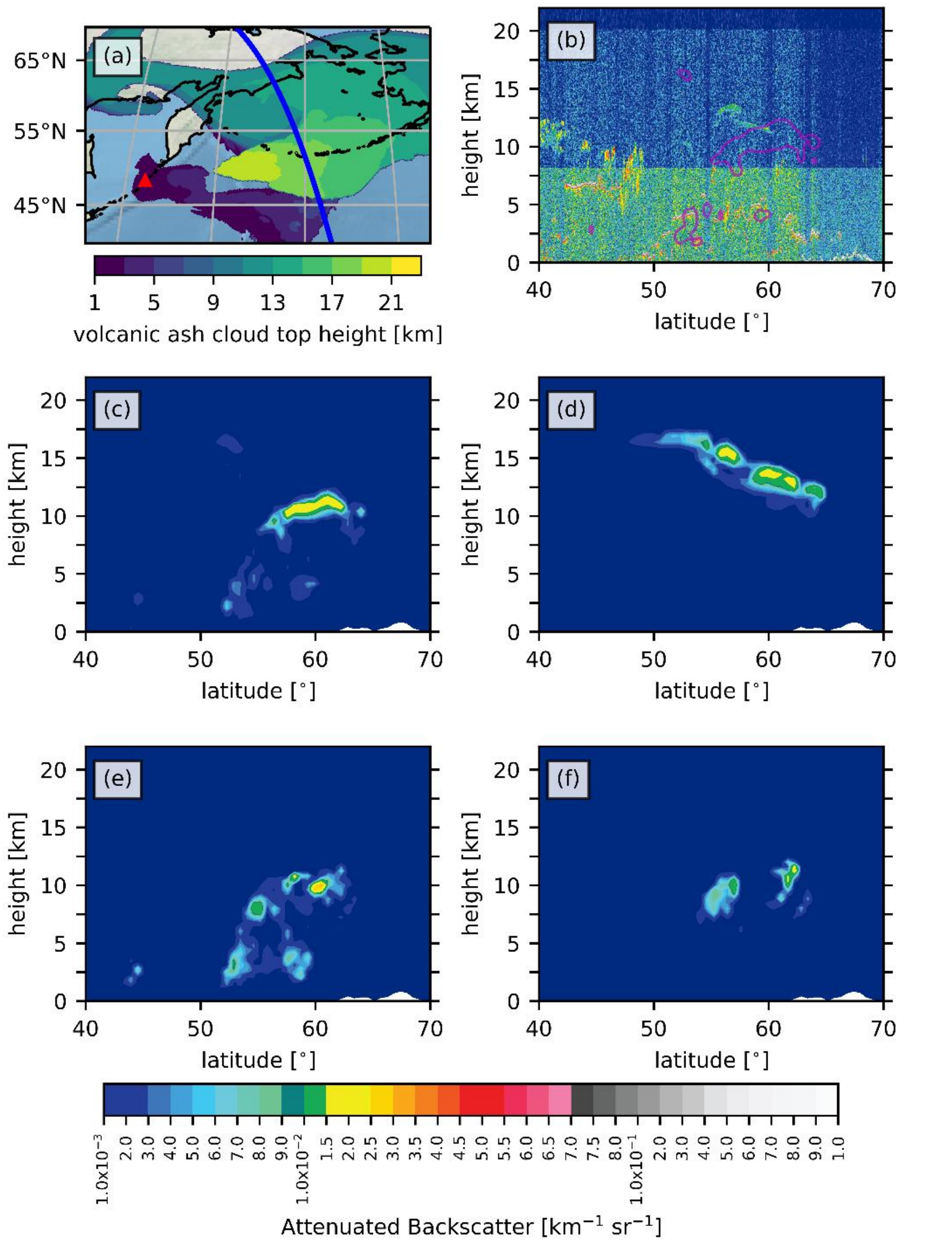

2019-06-25 01:00 UTC
(a) CALIPSO ground track and modeled volcanic cloud top height
(b) Total Attenuated Backscatter at 532 nm measured by CALIOP
(c) AERODYN – rad
(d) no AERODYN – rad
(e) AERODYN – no rad
(f) no AERODYN – no rad

11. Figure 7: Even if the model indeed do a better job by including the dynamics and radiation to remove ash, it does not capture well small-scale variations. Could you further explain why it's not the case? Maybe incorporating more accurate source terms based on HIMAWARI-8 would help with that.

This is a very good point. Although the overall agreement is very good, there are small-scale variations in the AHI retrieval that don't have a corresponding model result.
At this point we should distinguish between two periods, the eruption period, roughly during the first 12h, and the quiet period during which the volcano did not emit ash anymore.
In this study we emit volcanic ash with a constant emission rate over 9h. We know from satellite images (GEOS17, Himawari-8) that Raikoke emitted ash with several longer and shorter puffs. The last, rather short puff happened on 22 July 2019 at around 07:10 UTC. This explains well the offset between model result and observation, and also the small-scale variations in the observation during the eruption phase. Characterizing these puffs in terms of height and mass eruption rate (and thus time dependent eruption rate) is the topic of ongoing work.
After the eruption has stopped, the small-scale variations in the AHI retrieval are due to deficiencies or limitations of the retrieval algorithm, as any increase of measured ash cannot be associated with an emission.
In order to make this clearer in the manuscript, we add additional information to l.368.

As Raikoke did not erupt continuously over these 9 h, the offset between simulation and observation as well as the small-scale variations in the observation during this period can be explained.

Furthermore, we add one and rephrase one sentence in l. 373:
The small-scale variations in the observation might be due to deficiencies or limitations of the retrieval algorithm, as no new ash is emitted during this period. We can see a very similar decay and stabilization of ash mass for the AERODYN-rad scenario in green.

12. P17L375: It would be interesting to know which processes contribute to the removal of ash in the model. I believe the growth term that lead to the removal by sedimentation, what about ash-ice interaction and wet deposition?

In ICON-ART we account for sedimentation, dry deposition and wet deposition (scavenging by raindrops below clouds). These processes are active for all aerosols for all presented simulation cases, i.e. they are not exclusively linked to the AERODYN development. However, the presented setup of ICON-ART does not account for ash-ice interaction or CCN activation of aerosol yet. Combining aerosol aging with aerosol activation will be subject of future development.
In order to have this information in the manuscript as well, we add the following in l.184:

The removal of aerosols from the atmosphere is modeled by three different processes: sedimentation, dry deposition and wet deposition. In ICON-ART wet deposition describes scavenging by raindrops below clouds.

Furthermore, we discuss the differences of these three mechanisms in l. 377 ff.:
Additionally, we would like to note that the prevailing settling mechanism of aerosol after the Raikoke 2019 eruption for all our simulation scenarios is due to sedimentation. Dry

deposition is only relevant for aerosol near the ground. Wet deposition should also play a minor role during the first days after the eruption, as most of the volcanic ash is emitted above cloud level.

13. Figure 9: More data are needed to verify the model outputs. e.g. CALIPSO and OMPS.

As already discussed in our answer to comment 7, we were not able to retrieve additional meaningful OMPS-LP data for plume top heights.
In contrast, there exist several CALIPSO overpasses (which we show in our answer to comment 10). The measurements of total attenuated backscatter at 532 nm on these dates show a signal which can be associated with volcanic aerosol. However, in the scope of this work we were not able to define an objective quantity that allows us determining the volcanic cloud top height in CALIOP measurements. That is the reason why we constrain the comparison between CALIOP and ICON-ART to the more qualitative Fig. 6.

14. P20L431: I believe that measurement uncertainty from OMPS could be better addressed. The vertical resolution of the instrument is probably near 1-2 km. Could you add the corresponding error bar in figure 8. In addition, I'm pretty confident that additional information on volcanic cloud top height could be found by analyzing additional OMPS data.

The vertical sampling of OMPS-LP is 1km which gives us +/- 0.5km accuracy in the peak attribution. The remaining uncertainty in the pointing is about 0.2km. The latter is rather systematic. The aerosol retrieval has a vertical resolution of about 3km which smears the peak, however, won't displace it. This is why we estimate the measurement uncertainty with +/- 0.7km.
As suggested, we add an error bar to the OMPS-LP measurement in figure 8.

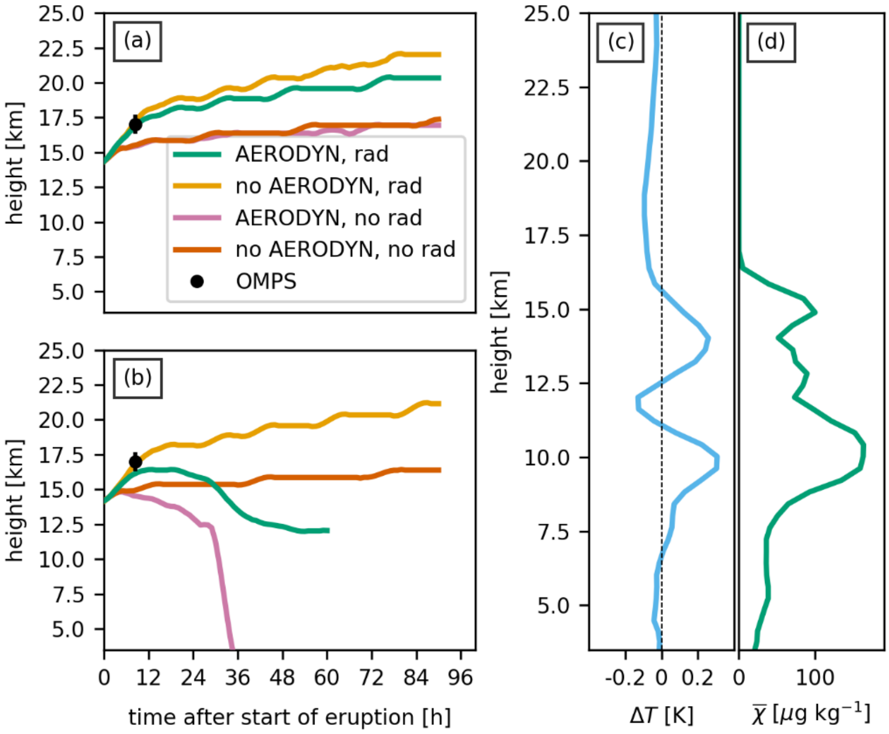

Figure 8. (a) and (b) Evolution of height of volcanic ash cloud top after the onset of the eruption on 21 June 2019, at 18:00 UTC. The yellow curve represents the no_AERODYN-rad scenario, the green curve AERODYN-rad, the pink one AERODYN-no_rad, and the orange one represents the no_AERODYN-no_rad scenario. Panel (a) shows the ash cloud top of particles in the accumulation mode, (b) of particles in the coarse mode, respectively. The black circle depicts the volcanic cloud top height obtained from OMPS-LP. (c) Mean temperature difference (AERODYN-rad – AERODYN-no_rad) in volcanic ash cloud columns on 23 June 2019, 12:00 UTC. (d) Mean volcanic ash concentration $\bar{\chi}$ for the same model columns as in (c) for AERODYN-rad.

Additionally, we add in l.161:

Due to uncertainties in pointing and vertical sampling we estimate the measurement error with +/- 0.7km.

Particle Aging and Aerosol–Radiation Interaction Affect Volcanic Plume Dispersion: Evidence from Raikoke Eruption 2019

Lukas O. Muser[1], Gholam Ali Hoshyaripour[1], Julia Bruckert[1], Akos Horvath[2], Elizaveta Malinina[3], Sandra ~~Peglow~~Wallis [4], Fred J. Prata[5], Alexei Rozanov[3], Christian von Savigny[4], Heike Vogel[1], and Bernhard Vogel[1]

[1]Institute of Meteorology and Climate Research, Karlsruhe Institute of Technology (KIT), Karlsruhe, Germany
[2]Meteorological Institute, University of Hamburg, Germany
[3]Institute of Environmental Physics, University of Bremen, Bremen, Germany
[4]Institute of Physics, Greifswald University, Greifswald, Germay
[5]AIRES Pty. Ltd., Mt Eliza, Victoria, Australia

Correspondence: Lukas O. Muser (lukas.muser@kit.edu)

Abstract. A correct and reliable forecast of volcanic plume dispersion is vital for aviation safety. This can only be achieved by representing all responsible physical and chemical processes (sources, sinks, and interactions) in the forecast models. The representation of the sources has been enhanced over the last decade, while the sinks and interactions have received less attention. In particular, aerosol dynamic processes and aerosol–radiation interaction are neglected so far. Here we address this gap by further developing the ICON-ART (ICOsahedral Nonhydrostatic – Aerosols and Reactive Trace gases) global modelling system to account for these processes.

We use this extended model for the simulation of volcanic aerosol dispersion after the Raikoke eruption in June 2019. Additionally, we validate the simulation results with measurements from AHI (Advanced Himawari Imager), CALIOP (Cloud-Aerosol Lidar with Orthogonal Polarization), and OMPS-LP (Ozone Mapping and Profiling Suite – Limb Profiler). Our results show that around $50\,\%$ of very fine volcanic ash mass (particles with diameter $d < 30\ \mu\mathrm{m}$) is removed due to particle growth and aging. Furthermore, the maximum volcanic cloud top height rises more than $6\ \mathrm{km}$ over the course of 4 days after the eruption due to aerosol–radiation interaction. This is the first direct evidence that shows how cumulative effects of aerosol dynamics and aerosol–radiation interaction lead to a more precise forecast of very fine ash lifetime in volcanic clouds.

1 Introduction

Volcanic aerosols pose significant hazards to aviation (Casadevall, 1994; Guffanti et al., 2010; Schmidt et al., 2014), and influence weather and climate (Robock, 2000; Mather, 2008). These aerosols are primarily composed of ash particles (tephra with diameter smaller than $2\ \mathrm{mm}$) (Rose and Durant, 2009). Secondary aerosols are generated from precursor gases, such as sulfate particles from SO_2, through chemical and microphysical processes (Tabazadeh and Turco, 1993; Textor et al., 2004; Durant et al., 2010).

During the first couple of days after the onset of an eruption, aerosol concentration can be locally so high that it jeopardizes air traffic. In the past, most of the aircraft damaging encounters occurred in spatial proximity ($< 1000\ \mathrm{km}$) to the volcano or within 24 hours after the onset of ash-producing eruptions (Guffanti et al., 2010). In order to provide a timely response to such events, a reliable forecast of volcanic aerosol dispersion is crucial. This is a challenging task because of large uncertainties in dispersion models mainly with respect to the eruption source parameters (e.g., mass eruption rate and plume height) and internal model parameterizations (e.g., wet deposition, aerosol dynamics, and optical properties) (Prata et al., 2019; von Savigny et al., 2020). While the model sensitivities to the source parameters were extensively studied in recent years (e.g. Mastin et al., 2009; Harvey et al., 2018), the role of the aerosol dynamics in plume dispersion remains largely unexplored.

Aerosol dynamic processes comprise nucleation, condensation, coagulation, and sedimentation. These processes alter the aerosol size and composition (particle aging) and thus, modify the optical properties of particles (Seinfeld and Pandis, 2016). Such changes eventually affect the aerosol dispersion and their interactions in the atmosphere ~~(Abdelkader et al., 2017; Yu et al., 2019).~~ (Abdelkader et al., 2017; Peterson et al., 2017; Yu et al., 2019). This can result in a lofting mechanism of aerosol which is different from the one caused by large scale atmospheric dynamics as described for example by Khaykin et al. (2017). Abdelkader et al. (2017) studied the sensitivity of transatlantic dust transport to chemical aging. The results show that chemical aging of dust particles increases the aerosol optical depth under subsaturated conditions and leads to regional radiative feedbacks to surface winds and dust emissions. Besides, the aged dust particles are removed more efficiently (by both wet and dry deposition) due to the increased hygroscopicity and particle size (Abdelkader et al., 2017). Peterson et al. (2017) observed in the Arctic near-surface atmosphere that the transport of atmospheric pollutants is influenced by active halogen chemistry. Yu et al. (2019) used modeling and satellite observations to characterize the effect of particle chemistry on smoke plume lofting after forest fires in Canada in August 2017. They reported that the smoke plume rose from 15 to 20 kilometers within 10 days owing to solar heating of aged black carbon.

Change of particle size during volcanic ash dispersion has been the topic of ash aggregation research in the last three decades (see Brown et al., 2012, and the references therein). Aerosol dynamics is one of the dominant mechanisms than lead to volcanic ash aggregation during long–range transport (Brown et al., 2012). Numerical models only (if at all) consider wet aggregation in the eruption column (Textor et al., 2006; Van Eaton et al., 2015; Folch et al., 2016; Marti et al., 2017). This can lead to an underestimation of the ash fallout and overestimation of airborne ash mass concentrations 1000s km from the volcano (Brown et al., 2012).

Previous works have studied the effects of aerosol–radiation interaction on the ash and SO_2 dispersion after historic eruptions assuming externally mixed aerosols (Niemeier et al., 2009; Schmidt et al., 2014). Niemeier et al. (2009) showed that the radiative effect of fine ash particles (strong absorption of shortwave and long-wave radiation) causes additional heating and cooling of ± 20 K per day and modifies the evolution of the volcanic cloud. Such impacts can be substantial in short-term at local scale and strongly depend on the optical properties of the volcanic particles (Niemeier et al., 2009; Timmreck, 2012; Vernier et al., 2016). It has been shown that volcanic ash particles interact and mix with other aerosols (Delmelle et al., 2007; Ayris and Delmelle, 2012; Bagnato et al., 2013; Hoshyaripour et al., 2015). This aging process affects the chemical composition and size distribution of the ash particles and can have a profound impact on their optical properties (Durant et al., 2010; Vogel et al., 2017). It is not clear yet how particle aging affects the dispersion and radiative impacts of volcanic ash. Here, we aim at exploring this gap by extending the ICON-ART (ICOsahedral Nonhydrostatic – Aerosols and Reactive Trace gases) global modelling system (Zängl et al., 2015; Rieger et al., 2015) by a new aerosol dynamic module named AERODYN (AEROsol DYNamics). This new extension allows us to investigate the formation of secondary aerosols and aerosol aging. In the scope of this paper we focus on timescales on the order of several days after the onset of an eruption. The primary focus is on the dynamics of the volcanic cloud during this initial period to provide information for volcanic aerosol dispersion forecasts. Therefore, we quantify the influence of secondary aerosol formation and particle aging on the optical properties of the volcanic particles. The research questions are as follows: 1) What is the influence of aerosol dynamics and ash aging on volcanic aerosol dispersion? 2) What is the effect of aerosol–radiation interaction on volcanic aerosol dispersion? 3) Are the representations of aerosol dynamics and aerosol–radiation interaction beneficial for volcanic aerosol dispersion forecast?

To answer these questions we investigate the Raikoke eruption in June 2019. The Raikoke volcano ($48.29°$ N, $153.24°$ E) is a stratovolcano located on Raikoke island, one of the central Kuril islands in the Sea of Okhotsk. An eruption started on June 21, 2019, at 18:00 UTC (Sennet, 2019). The large ash plume rapidly rose to 8–14 km altitude. A series of nine explosive events occurred until 05:40 UTC on 22 June. Forty airplanes were diverted because of the ash plume produced by this eruption (Sennet, 2019).

The paper is structured as follows: in Sect. 2 we present the observational data used in this study. Furthermore, the ICON-ART modeling system is described together with the simulation setup. Section 3 presents the results and the discussion of the very. Answers to the posed research questions are given in Sect. 4.

2 Methodology

2.1 Observation data

2.1.1 SO_2 from TROPOMI

The spread of the SO_2 plume ejected by the Raikoke eruption in June 2019 as well as the amount of released SO_2 mass was investigated by analyzing SO_2 total vertical column densities from the hyperspectral nadir-viewing TROPOspheric Monitoring Instrument (TROPOMI) aboard the Sentinel-5 Precursor satellite. TROPOMI provides daily global coverage completing 14.5 orbits every day (van Kempen et al., 2019) with a pixel size of $7\ \mathrm{km} \times 3.5\ \mathrm{km}$ (Theys et al., 2019). TROPOMI SO_2 (daylight only) offline level 2 data were downloaded from the Copernicus website (https://s5phub.copernicus.eu). The total vertical SO_2 column densities used, assume a SO_2 profile described by a $1\ \mathrm{km}$ thick box at $15\ \mathrm{km}$ altitude to account for explosive volcanic eruptions (Theys et al., 2017).

A self-defined geographic grid including the area from $30°$ N – $75°$ N and $135°$ E – $120°$ W with a resolution of $0.1° \times 0.1°$ was created. The SO_2 cloud expansion for every TROPOMI orbit was visualized by first averaging all vertical SO_2 column densities inside a single grid segment and multiplying the result by the SO_2 molar mass in order to obtain a mass loading in units of $\mathrm{g\,m^{-2}}$. Only data with ~~the quality descriptor 'qa_value '~~ a quality value larger than 0.5 (as recommended in the TROPOMI product user manual) and total vertical column density with values less than $1000\ \mathrm{mol\,m^{-2}}$ were used.

The SO_2 mass loading for each grid segment was multiplied subsequently with the associated grid segment area to obtain the SO_2 mass in units of g. The total SO_2 mass for the observed area was determined for the observed area over time periods of approximately 24 h, i.e., by averaging batches of 14 consecutive orbits for every single grid segment. Finally, the mass is summed up over the entire grid. The described data averaging was applied because consecutive orbits partially overlap. This method suggests a total emitted SO_2 mass of $(1.37 \pm 0.07) \times 10^9$ kg over the course of the Raikoke eruption 2019. Since the air mass factor used in the retrieval of the vertical column densities depends on the ~~SO2~~ SO_2 vertical distribution, the choice of the assumed SO_2 profiles ~~seem~~ seems to be the most important source of error. ~~The stated uncertainty~~ It remains, however, a non-trivial challenge to estimate the associated uncertainty of the SO_2 mass calculation. The uncertainty stated above reflects the average absolute difference between the SO_2 mass calculated from an assumed SO_2 profile peak in 15 km and 7 km altitude, respectively. SO_2 masses from 20 June, 16:41 UTC to 6 July, 10:08 UTC were included in the averaging.

2.1.2 Ash and SO_2 from Himawari-8

Himawari-8 is a geostationary satellite platform operated by the Japanese Space Agency (JAXA) in collaboration with the Japanese Meteorological Agency (JMA) carrying the 16 band visible and infrared Advanced Himawari Imager (AHI). Data are acquired every 10 minutes over the Earth's disc covering a circular field of view of approximately 70 degrees, centred at the equator and $\sim 140°$ E longitude. Further details of the orbit, instrument, duty cycles, image geolocation, and data calibration can be found on the JAXA/JMA website and in documentation (https://www.data.jma.go.jp/mscweb/en/himawari89/space_segment/spsg_ahi.html).

For the purpose of this work, AHI infrared data were analysed at 10 min intervals to determine the column amounts of SO_2 gas and ash particle mass loadings, both in units of $\mathrm{g\,m^{-2}}$. At the sub-satellite point the nominal spatial resolution of infrared pixels is $4\ \mathrm{km}^2$, increasing to $> 100\ \mathrm{km}^2$ at the largest scan angles. The Raikoke plume covered a relatively large geographic region and range of latitudes/longitudes, so the data were first rectified and resampled to a grid of 1336×2139 latitude $\times$ longitudes centred at $52.5°$ N latitude and $175°$ E longitude using a stereographic projection. These infrared data were then processed to determine SO_2 and ash amounts at 10 min intervals. The final data were analyzed at both 10 min and hourly intervals. The basis of the retrieval of SO_2 slant column amount relies on using AHI band 10 centred near to 7.3 µm. At this wavelength there is a strong SO_2 absorption band. ~~Unfortunately, water vapour~~ Water vapor and clouds cause interference with the SO_2 signal ~~so a~~ and introduce a positive bias. Therefore, a retrieval scheme was devised to minimize the interfering effects. In short, the bias is minimized by subtracting an offset SO_2 retrieval for a small region where no SO_2 is believed to exist. Details of the retrieval method are very similar to a scheme devised for the High Resolution Infrared Sounder (HIRS) data described by Prata et al. (2003).

Volcanic ash effective particle radius and optical depth are retrieved using AHI bands 14 (~ 11.2 µm) and 15 (~ 12.4 µm) on the same latitude/longitude grid as that used for SO_2. The basic physics has been described by Prata (1989) and the retrieval methodology has been described by Prata and Prata (2012) using Meteosat Second Generation (MSG) Spin-Enhanced Visible and Infrared Imager (SEVIRI) data, which has very similar characteristics to the AHI data used here.

Discussions of potential error sources in ash retrieval can be found in numerous papers in the literature, e.g., Wen and Rose (1994); Prata et al. (2001); Clarisse et al. (2010); Mackie and Watson (2014); Western et al. (2015). Prata and Prata (2012) and Clarisse and Prata (2016) provide some error estimates based on independent validation which suggest single pixel retrievals have an absolute error of $\pm 0.5\ \mathrm{g\,m^{-2}}$ with a low bias; however, much larger errors and biases can occur on occasion and it is generally accepted that relative errors typically lie between 40–60 %. Single pixel retrievals $< 0.2\ \mathrm{g\,m^{-2}}$ are regarded as at the threshold of detection. The presence of ice reduces the ash mass estimates by an amount that depends on the proportion of the pixel covered by ice. However, during the Raikoke eruption, ice was not observed except possibly at the start of the eruption which could cause lower ash mass estimates.

The retrieval assumes that pixels detected as containing ash are completely ash covered and although meteorological cloud tests are used, inevitably some anomalous retrievals occur. To minimise these, a mask was used whereby all pixels falling outside a $0.1\ \mathrm{g\,m^{-2}}$ contour line are removed. Within the $0.1\ \mathrm{g\,m^{-2}}$ contour, a 9×9 median filter was applied to remove any remaining “spikes”. These measures are largely cosmetic and are based on the premise that anomalous pixels appear to be unphysical in nature. Integrating the horizontal mass loadings for volcanic ash and SO_2 their emitted masses can be estimated. Based on the AHI measurements the total emitted very fine ash mass ($d < 32\ \mathrm{\mu m}$) ranges between $0.4\text{–}1.8 \times 10^9\ \mathrm{kg}$, the SO_2 mass between $1\text{–}2 \times 10^9\ \mathrm{kg}$. The latter agrees well with the TROPOMI measurement in Sect. 2.1.1.

2.1.3 Volcanic cloud height from MODIS, VIIRS, OMPS, and CALIOP

There are several ways of obtaining volcanic cloud top heights in the upper troposphere and lower stratosphere. In this work, we use data from four spaceborne instruments, MODIS (Moderate Resolution Imaging Spectroradiometer), VIIRS (Visible Infrared Imager Radiometer Suite), OMPS-LP (Ozone Mapping and Profiling Suite – Limb Profiler), and CALIOP (Cloud-Aerosol Lidar with Orthogonal Polarization). These instruments are briefly described in the following.

We used meteorological cloud top height (CTH) and volcanic ash cloud top height retrievals from MODIS aboard the Terra and Aqua satellites and VIIRS aboard the S-NPP (Suomi National Polar-orbiting Partnership) and NOAA-20 satellites. These polar–orbiting instruments observed Raikoke on 22 June 2019, at 01:25 UTC (Terra and NOAA-20), 02:15 UTC (S-NPP), and 03:10 UTC (Aqua and NOAA-20) when a brownish–colored and still localized plume was largely distinguishable from white/gray meteorological clouds in visible channel images. MODIS cloud top height, available at $1\ \mathrm{km}$ horizontal resolution, is obtained by matching the retrieved cloud top pressure to a Numerical Weather Prediction (NWP) geopotential height profile (Menzel et al., 2015). For the Raikoke plume, classified essentially as ice phase with a few liquid phase pixels, cloud top pressure was mostly determined by the CO_2–slicing technique from channels near $13\ \mathrm{\mu m}$ and to a lesser degree by the infrared window technique from the $11\ \mathrm{\mu m}$ channel. For VIIRS, on the other hand, cloud top height was determined only from the 8.5, 11, and $12\ \mathrm{\mu m}$ channels, because the instrument lacks CO_2 absorbing channels. The NOAA Enterprise AWG (Algorithm Working Group) Cloud Height Algorithm (ACHA) first determines cloud top temperature (CTT) from these midwave infrared channels using an optimal estimation framework and then matches CTT to a collocated NWP temperature profile (Heidinger and Li, 2019). The VIIRS CTHs are available at $750\ \mathrm{m}$ horizontal resolution. In addition to the meteorological cloud products, VIIRS retrievals by a dedicated volcanic ash detection and height algorithm (Pavolonis et al., 2013) were also utilized. The optimal estimation method is based on the same midwave infrared channels as used in the cloud retrievals, but the underlying microphysical models assume particles (andesite, quartz, kaolinite, or gypsum) that are better suited for volcanic plumes than liquid water or ice. A series of spectral and spatial tests first select only those pixels that potentially contain volcanic ash, which makes retrieval coverage more restricted compared to the standard cloud product, especially in scenes containing a mix of ash and water clouds. The algorithm then retrieves ash cloud effective temperature and effective emissivity, from which ash cloud height is computed with the help of NWP temperature profiles. The estimated ash height error was typically 1–2 km for the Raikoke plume. Despite their different assumptions about plume microphysics, the cloud and ash height retrievals agreed well where both were produced and indicated a maximum plume top height between 12–12.6 km about 8 h after the start of the eruption.

The volcanic cloud top height on 22 June 2019, was determined by visual analysis of the stratospheric aerosol extinction coefficient profiles from the OMPS-LP instrument. Here, the aerosol extinction coefficient product at 869 nm (V1.0.9) retrieved at the University of Bremen is used. The OMPS aerosol extinction coefficient was retrieved on a 1 km grid from 10.5 to 33.5 km with the algorithm adapted from the SCIAMACHY V1.4 (Rieger et al., 2018). The retrieval is done under the assumption that stratospheric aerosol is represented by spherical sulfuric droplets with a unimodal log–normal particle size distribution ($r_{med} = 80$ nm, $\sigma = 1.6$). Due to uncertainties in pointing and vertical sampling we estimate the measurement error with ± 0.7 km. Detailed information on the retrieval algorithm can be found in Malinina (2019) and Malinina et al. (2020). Here, it should be noted that the evaluation of the plume top height from OMPS-LP was possible only on the 22 June 2019. On that day, the instrument was passing right above the Raikoke island, and the plume was very localized. Thus, the increase in the aerosol extinction coefficient associated with the eruption was large and obvious. This large increase was a result of a vast amount of ash released with the eruption. In the following days, when the plume started to spread over the North Pacific, the ~~unique attribution of the observed values to the Raikoke eruption is not possible anymore. At this point any increased extinction can be caused both by the Raikoke eruption and by any other interfering event, such as~~ core of the fresh plume is not hit by the OMPS-LP instrument sampling anymore. Slightly perturbed aerosol extinction observed in transition regions has a similar magnitude as that from interfering events, e.g., the aerosol transport from the Ambae eruption ~~, which occured~~ that occurred 11 months earlier~~.~~, and thus cannot be attributed exclusively to the Raikoke eruption. For this reason, we excluded the OMPS-LP measurements in transition regions from the consideration.

CALIOP is one of three instruments on board the CALIPSO (Cloud-Aerosol Lidar and Infrared Pathfinder Satellite Observation) satellite, which was launched on 28 April 2006 and is still operational. CALIOP provides backscatter measurements at 532 nm and 1064 nm and the backscattered radiation at 532 nm is measured in two channels detecting orthogonally polarized radiation. The determination of the Raikoke plume height is based on total attenuated backscatter data at a wavelength of 532 nm. CALIOP L1 data version 4.10 is used.

In the scope of this paper, we analyze the CALIPSO overpass on 23 June 2019, at around 15:00 UTC. On this date the total attenuated backscatter at 532 nm shows a distinct feature between 15 and 16 km that can be associated with the volcanic cloud.

2.2 Modeling system and set up

2.2.1 ICON-ART modeling system

This study uses the ICOsahedral Nonhydrostatic weather and climate model with Aerosols and Reactive Trace gases (ICON-ART). ICON is a non-hydrostatic modeling system that solves the full three-dimensional non-hydrostatic and compressible Navier–Stokes equations on an icosahedral grid (Zängl et al., 2015). ICON can be used for seamless simulations of various processes across local to global scales (Heinze et al., 2017; Giorgetta et al., 2018). The ART module is an extension of ICON to account for emission, transport, physicochemical transformation, and removal of the trace gases and aerosols in the troposphere and stratosphere (Rieger et al., 2015). Zängl et al. (2015), Rieger et al. (2015), and Schröter et al. (2018) provide detailed technical descriptions of ICON and ICON-ART, respectively. The removal of aerosols from the atmosphere is modeled by three different processes: sedimentation, dry deposition and wet deposition. In ICON-ART wet deposition describes scavenging by raindrops below clouds.

The Rapid Radiative Transfer Model (RRTM) (Mlawer et al., 1997) is used in ICON as the standard radiation scheme for numerical weather prediction. To account for the aerosol radiative effect, ART calculates the local radiative transfer parameters (extinction coefficient, single scattering albedo, and asymmetry parameter) based on the optical properties and the prognostic mass concentration of aerosols at every grid point and for every level. These are then used as the input parameters for the RRTM scheme (Gasch et al., 2017). This approach ensures full coupling and feedback between aerosol processes, radiation and the atmospheric state (Shao et al., 2011). Besides, a forward operator is implemented in the model to diagnose the attenuated backscatter at the wavelengths 532 and $1064\ \mathrm{nm}$ (Hoshyaripour et al., 2019). To account for secondary aerosol formation and internally mixed aerosols, a new aerosol dynamics module is currently developed and implemented in ICON-ART. Details of this module are described in the following section.

2.2.2 Aerosol dynamics

The aerosol dynamics module (AERODYN) includes 10 log–normal modes that consider Aitken, accumulation and coarse particles in soluble, insoluble and mixed states plus a giant insoluble mode. This new development allows a very flexible combination of different species for different ICON-ART applications. The Aitken, accumulation, coarse (in all mixing states) and giant modes are initialized with geometric median diameter of 0.01, 0.2, 2.0 and $12.0\ \mu\mathrm{m}$ and standard deviations of 1.7, 2.0, 2.2 and 2.0, respectively. Figure 1 provides additional information about the organization of the modes and species in AERODYN.

For each mode prognostic equations for the number density and the mass concentration are solved while the standard deviations are kept constant. The generalized aerosol dynamics equations have the following form:

$$\frac{\partial}{\partial t}M_{0,i} = -Ca_{0,ii} - Ca_{0,ij} + Nu_0 \quad (1)$$

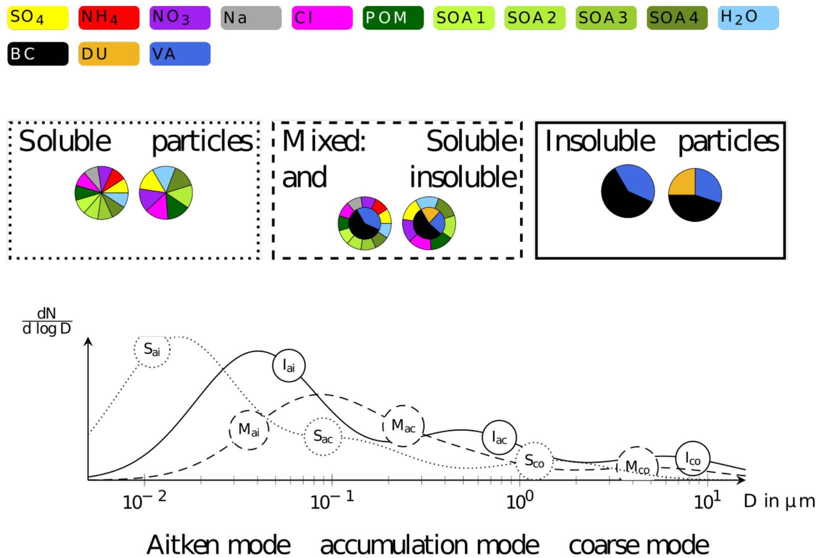

Figure 1. Chemical composition of the soluble (first row) and insoluble (second row) modes, mixing state of the modes (third row) and particle size distribution (giant mode is not shown). The dotted line represents a particle size distribution of soluble particles, the dashed line of mixed particles, and the solid line of insoluble particles, respectively. POM: primary organic matter, SOA: secondary organic aerosols, BC: black carbon. DU: desert dust, VA: volcanic ash. Upper panel adopted from Kaiser et al. (2014). In the current work, insoluble mode contains volcanic ash only while soluble mode contains only SO_4^{2-} and H_2O.

$$\frac{\partial}{\partial t} M_{3,i} = -Ca_{3,ij} + Co_{3,i} + Nu_3 \tag{2}$$

where $M_{0,i}$ and $M_{3,i}$ describe the zeroth (number density) and third (mass concentration) moment of mode i, respectively. The terms Ca, Co and Nu refer to coagulation, condensation and nucleation, respectively. The terms $Ca_{m,ii}$ and $Ca_{m,ij}$ are intra and inter-modal coagulation in the moment m, respectively. Nucleation is considered for the Aitken mode only. Condensation and coagulation affect all modes except the giant mode. The nucleation, condensation and coagulation terms are calculated following Riemer et al. (2003) and Vogel et al. (2009). Furthermore, ISORROPIA II model is used to calculate the gas-aerosol partitioning according to thermodynamic equilibrium (Fountoukis and Nenes, 2007).

Shifting between modes is performed using two mechanisms. The first mechanism is activated when a threshold diameter is exceeded. Then, a shift to a corresponding mode with larger median diameter is performed. The second mechanism shifts mass and number concentration from insoluble modes to mixed modes if a mass threshold of soluble coating on insoluble particles (currently 5 %) is exceeded (Weingartner et al., 1997).

2.2.3 Aerosol optical properties

The RRTM requires the mass extinction coefficient k_e, single scattering albedo ω, and asymmetry parameter g in 30 wavelength bands to account for the radiative effect of aerosols (Gasch et al., 2017). In this connection, k_e can be interpreted as the extinction cross-section per aerosol mass in the units $\mathrm{m}^2\,\mathrm{kg}^{-1}$.The wavelength bands range between 0.2 and 100 µm. The calculation of the optical properties is based on the wavelength-dependent refractive indices of volcanic ash (Walter, 2019), water, and sulfuric acid (Gordon et al., 2017).

No study so far has treated volcanic ash as a core in an internal mixture. It is suggested, but not proven, that most volcanic ash particles are coated to some degree (Bagnato et al., 2013; Hoshyaripour et al., 2015). Therefore, the core-shell treatment is physically more realistic than the external-mixture treatment even though the reality lies between the externally mixed and core treatments (Jacobson, 2000; Riemer et al., 2019). Hence, this study deploys both externally mixed (in the soluble and insoluble modes) and internally mixed (in the mixed mode) treatments. For the mixed mode, we use the core-shell model in which the core and shell consist of well-mixed volcanic ash and H_2O-H_2SO_4 solution, respectively. To calculate the optical properties, the Mie code for coated spheres is used which has been developed by Mätzler (2002) and Bond et al. (2006) based on Bohren and Huffman (1983). Based on the ICON-ART simulations the shell fraction (increased diameter due to coating) is assumed to be 0.2 with 50 % H_2O-H_2SO_4 solution. The volume-average mixing rule is used to compute the complex refractive index of each layer, which then serves as input for the core-shell calculation.

The results of the Mie calculations for the ash-containing modes are shown in Fig. 2. It can be seen that the mixed modes (coated ash) have higher k_e and ω in the visible range than the insoluble modes (uncoated ash). This is caused by the H_2O-H_2SO_4 coating which is a strong scatterer. Particles with a strongly absorbing core coated by a weak absorber generally absorb more sunlight than an external mixture of the same components, which is caused by the increase of the core cross section due to coating (Jacobson, 2000). This is not the case for volcanic ash as it is not a strong absorber compared to soot particles. This can be seen in the imaginary part of refractive indices, i.e., absorbing part, at 500 nm that are 0.00092 and 0.74 for volcanic ash and soot, respectively.

The Mie theory assumes that the particles have spherical shapes. In reality, volcanic ash particles are exclusively non-spherical particles (Bagheri and Bonadonna, 2016). Therefore, their optical properties may be better represented by spheroids, ellipsoids or even more complex structures (Gasteiger et al., 2011; Vogel et al., 2017). However, the liquid coating can lead to spherical particle surfaces, which justifies the assumption of the particle sphericity in the mixed mode. For consistency reasons, the sphericity assumption is also applied to the insoluble mode that contains uncoated ash particles. Implementing coated non-spherical ash particles into ICON-ART remains the subject of future work.

2.2.4 Model configuration

In the scope of this study we performed ~~three~~ four global simulations with the ICON-ART model. The simulations run on a R3B07 grid that is also used by the German Meteorological Service (DWD) for operational weather forecasts. The horizontal grid resolution is on average $\Delta\bar{x} = 13.2$ km. 90 vertical levels resolve the atmosphere up to 75 km. The time step Δt is 60 s.

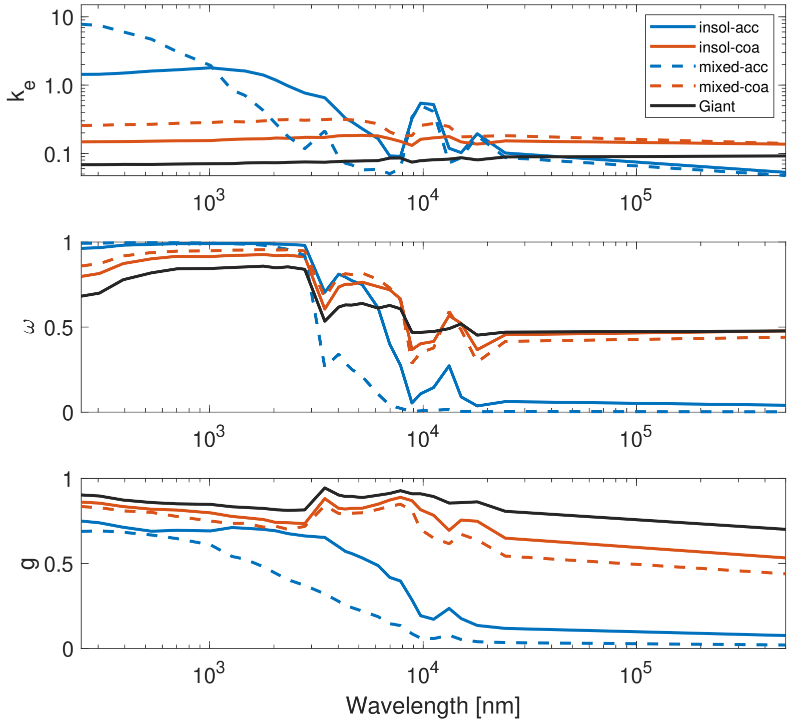

Figure 2. Optical properties of the ash-containing modes at RRTM wavelengths. k_e has the unit $\mathrm{m}^2\ \mathrm{g}^{-1}$. ω and g are unitless. Insoluble and mixed states are shown by solid and dashed lines while accumulation and coarse sizes are demonstrated with blue and red colors, respectively.

Each simulation is started on 21 June 2019 at 12:00 UTC based on initialized analysis data provided by DWD. The simulation covers the first four days after the onset of the eruption.

The volcanic emission starts on 21 June 2019, at 18:00 UTC and lasts $9\ \mathrm{h}$. The simulated Raikoke eruption emits ash particles and SO_2. In the model the emission is characterized by an emission height and emission rate which we derived from a combined approach of satellite measurements and 1D plume simulations.

The plume height estimate is based on the MODIS and VIIRS data shown in Fig. 3. The dedicated ash algorithm (lower panel) is much more restrictive than the standard cloud-top height algorithm (upper panel), but produces similar heights where it is applied. In general, both of these brightness temperature-based products indicate maximum plume heights in the 12–$12.6\ \mathrm{km}$ range for the time period 7–$9\ \mathrm{h}$ after the eruption. The estimated height uncertainty is $\sim 1.5\ \mathrm{km}$. Based on this plume height estimate and also other studies (Sennet, 2019), the Raikoke eruption emits ash and SO_2 in our simulations at a constant eruption rate between 8 and $14\ \mathrm{km}$ above sea level.

The eruption rate of SO_2 is derived from measurements of the total emitted SO_2 mass. According to the TROPOMI (Sect. 2.1.1) and AHI data (Sect. 2.1.2), in our simulation $1.5 \times 10^9\ \mathrm{kg}$ of SO_2 is emitted over the eruption period. To estimate the

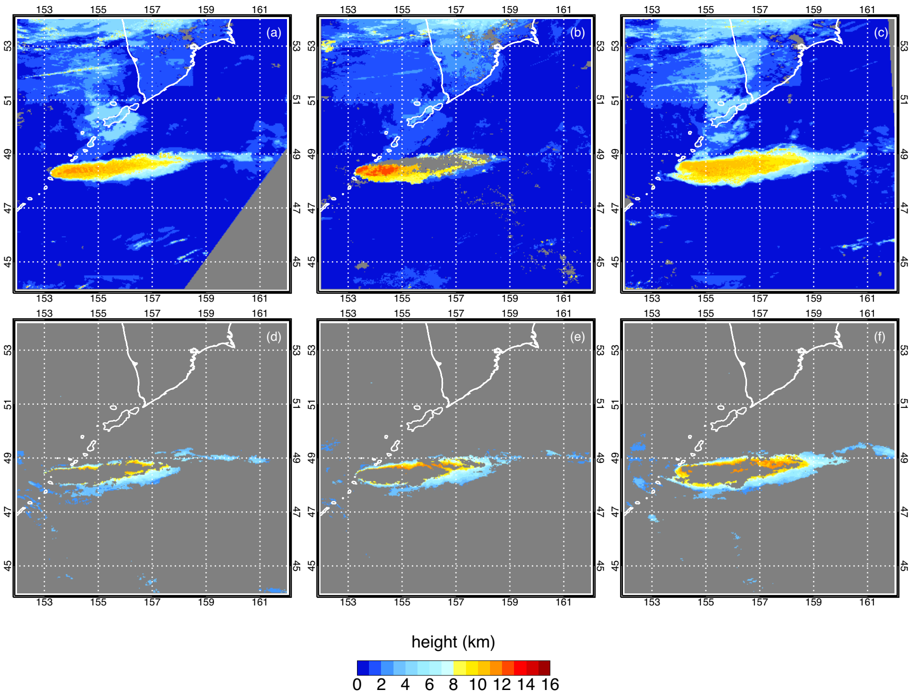

Figure 3. Plume height on 22 June 2019, at 01:25 UTC ((a) and (d)), 02:15 UTC ((b) and (e)), and 03:10 UTC ((c) and (f)). The top row shows standard cloud-top heights for (a) MODIS Terra, (b) VIIRS Suomi-NPP, and (c) MODIS Aqua. The bottom row plots ash heights from NOAA's dedicated volcanic ash algorithm for VIIRS on ((d) and (f)) NOAA-20 and (e) Suomi-NPP, considering only those pixels that potentially contain volcanic ash.

total mass eruption rate of volcanic ash, several 1D plume simulations using Plumeria (Mastin, 2007) and FPlume (Folch et al., 2016) are conducted assuming the following parameter ranges: plume height $12–14\ \mathrm{km}$, vent diameter $90–110\ \mathrm{m}$, exit velocity $100–120\ \mathrm{m\,s^{-1}}$, exit temperature $900–1100\,^{\circ}\mathrm{C}$, and exit gas mass fraction 3 %. For this purpose, atmospheric profiles are obtained from ERA-Interim (Dee et al., 2011) and introduced in the 1D models as wind and no-wind atmospheres. By this method, the key sources of uncertainty are considered in the estimation of mass eruption rate. The results are in the range of $1.45–9.95 \times 10^6\ \mathrm{kg\,s^{-1}}$. Taking the mean value $5.7 \times 10^6\ \mathrm{kg\,s^{-1}}$ suggests that about $190 \times 10^9\ \mathrm{kg}$ tephra is emitted within 9 hours. Assuming that 1 % of the erupted mass is very fine ash with $d < 30\ \mathrm{\mu m}$ (relevant for long range transport) (Rose and Durant, 2009; Gouhier et al., 2019), we estimate that $1.9 \times 10^9\ \mathrm{kg}$ very fine ash is injected into the atmosphere during the eruption. The estimates by the 1D models are in agreement with AHI data (Sect. 2.1.2).

The estimated $1.9 \times 10^9\ \mathrm{kg}$ of very fine ash are used in the ICON-ART simulations and distributed equally between accumulation, coarse, and giant modes. The number concentration of the log–normal distribution is calculated based on the median diameter d_e and standard deviation σ_e of the emitted particle distribution. Table 1 lists details about these emitted particle size distributions. They are based on data from Bonadonna and Scollo (2013).

Table 1. Emission parameters for ash emission with median diameter d_e and standard deviation σ_e of ash size distribution, and the mass emission rate Q_e of each ash mode and SO_2.

Ash mode	Accumulation	Coarse	Giant	SO_2
d_e [µm]	0.8	2.98	11.35	–
σ_e [-]	1.4	1.4	1.4	–
Q_e [$\mathrm{kg\,s^{-1}\,m^{-1}}$]	3.26	3.26	3.26	7.72

We study the effect of aerosol dynamic processes and the radiative effect of internally mixed particles on the volcanic plume dispersion with the help of ~~three~~ four different simulation scenarios summarized in Table 2. The first scenario (AERODYN-rad) uses the whole new development of the AERODYN module together with the radiative feedback of internally mixed particles. In the second scenario (no_AERODYN-rad) only insoluble ash particles of three different size ranges are transported. Secondary aerosol formation and particle aging are switched off. However, the volcanic ash still interacts with solar and thermal radiation. The third scenario (AERODYN-no_rad) considers the effects of aerosol aging without any radiative feedback of these particles. The fourth scenario represents the status quo of operational volcanic cloud forecast. It considers neither aerosol dynamic effects nor aerosol-radiation interaction.

The two scenarios with AERODYN treat SO_2 as a chemical substance which can be oxidized. The chemical reaction scheme is a simplified OH-chemistry scheme that has been implemented into ICON-ART by Weimer et al. (2017). The no_AERODYN ~~scenario treats~~ scenarios treat SO_2 as a passive tracer without any gas phase chemistry.

Table 2. Simulation scenarios with their represented processes.

scenario	aerosol dynamics and gas phase chemistry	aerosol–radiation interaction
AERODYN-rad	on	on
no_AERODYN-rad	off	on
AERODYN-no_rad	on	off
no_AERODYN-no_rad	off	off

3 Results and Discussion

3.1 Ash and SO_2 transport

We compare our model results with different satellite products as introduced in Sect. 2.1. Figure 4 (a) and (b) show daily mean AHI retrievals of volcanic ash mass loading. As described earlier, the filtered data is used. For the daily mean only ash containing pixels are considered. The same averaging approach we apply on the ICON-ART model results, shown in panels (c) to (f) of Fig. 4. Panels in the left column show measurements and model results of 22 June 2019, panels in the right column

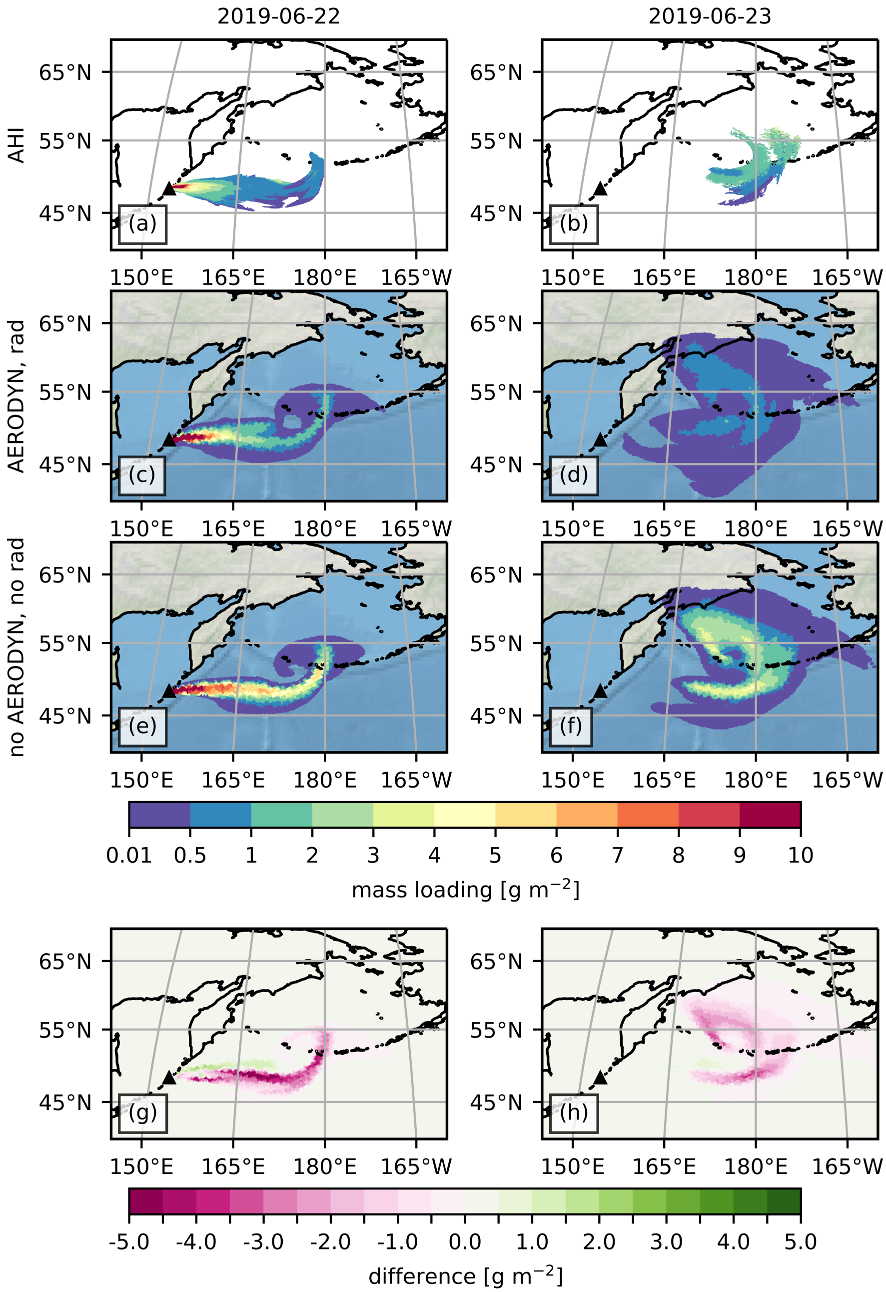

Figure 4. Daily mean total column mass loading of volcanic ash on 22 June (left column) and 23 June 2019 (right column). Top row (panel (a) and (b)) shows results measured by AHI on-board Himawari-8. The middle and lower row (panel (c) – (f)) show ICON-ART results for AERODYN-rad and no_AERODYN-no_rad, respectively. The black triangle depicts the location of Raikoke volcano. Panels (g) and (h) show the absolute difference between the two simulation scenarios.

of 23 June, respectively. On 22 June the volcanic cloud moved eastward towards 180° E where the direction of transport turned northward. The maximum of daily mean mass loading is still located in proximity to the volcano. For this day, both model results and the satellite retrieval agree very well in location, structure, and absolute values of ash mass loading. We can assume that the model captures the atmospheric state well, one day after its initialization. Furthermore, there are only minor differences between the two different simulation setups for the results of 22 June in Fig. 4 (c) and (e). These differences are mainly restricted to the slightly higher mass loading in panel (e) and small differences in the volcanic cloud structure. For the first day after the eruption, the aerosol dynamic effects and the aerosol–radiation interaction ~~has no significant~~ have only a minor influence on the volcanic ash mass loading. On 23 June the averaged AHI measurements show a more fragmentary ash distribution in Fig. 4 (b). This might be a result of volcanic cloud dilution in combination with deficiencies in the volcanic ash measurement of opaque regions. Most of the ash is measured between 50–55° N and around 180° E. The simulation results in Fig. 4 (d) and (e) support the assumption of the diluted volcanic cloud, as the mass loading only shows values smaller than ~~2~~ 4 $\mathrm{g\,m^{-2}}$. For both simulated scenarios, the overall structure of the volcanic cloud is similar. However, differences prevail in location and absolute values of maximum mass loading. These differences are due to aerosol dynamics and radiative effects which are addressed in more detail in Sect. ~~3.3~~3.2 and Sect. 3.3, respectively. Compared to these two simulations, the averaged AHI measurements (Fig. 4 (b)) ~~shows slightly higher~~ show values for the maximum ash mass loading ~~. This could be an artifact of the averaging approach, as it favors single pixels with high values for patchy retrievals.~~ that lie in between the two simulation scenarios. In panels (g) and (h) the differences between the two are highlighted by the absolute difference of AERODYN-rad – no_AERODYN-no_rad. It shows that considering aerosol dynamics and aerosol-radiation interaction results in lower volcanic ash mass loadings in most parts of the volcanic cloud. Only for the first day after the eruption, the volcanic cloud seems to be shifted slightly north in the AERODYN-rad scenario compared to the no_AERODYN-no_rad scenario, as the difference plot shows some positive values between 160–170° N.

In order to compare our ICON-ART results in an objective manner with the AHI observations, we make use of the SAL method. This quality measure has been introduced by Wernli et al. (2008) and has been extensively discussed by Wernli et al. (2009). The method identifies objects in a 2D field (e.g., total ash mass loading) and quantifies the differences between model and observation in structure (S), amplitude (A), and location (L). A value of 0 implies perfect agreement. We apply the SAL

Table 3. Comparison of daily mean total column mass loading of volcanic ash between AHI and ICON-ART results using the SAL method by Wernli et al. (2008).

	2019-06-22			2019-06-23		
scenario	S	A	L	S	A	L
AERODYN-rad	−0.191	0.584	0.004	1.651	0.298	0.041
AERODYN-no_rad	−0.323	0.579	0.002	1.362	0.275	0.028
no_AERODYN-rad	−0.202	0.921	0.014	1.601	0.716	0.031
no_AERODYN-no_rad	−0.270	0.874	0.013	1.546	0.748	0.030

method with a fix threshold value to identify objects $R^* = 0.01\,\mathrm{g\,m^{-2}}$. The results for the comparison of daily mean total column mass loading between the AHI retrieval and the ICON-ART results are summarized in Table 3. The location of the volcanic cloud agrees very well with the observation for all dates in all simulation scenarios. The structure of the volcanic cloud shows larger differences compared to observations, especially on 23 June. However, the values are rather similar for the different simulation scenarios. Only the amplitude values differ distinctly among the different scenarios. Simulations with AERODYN are closer to the observation than simulations without aerosol dynamics.

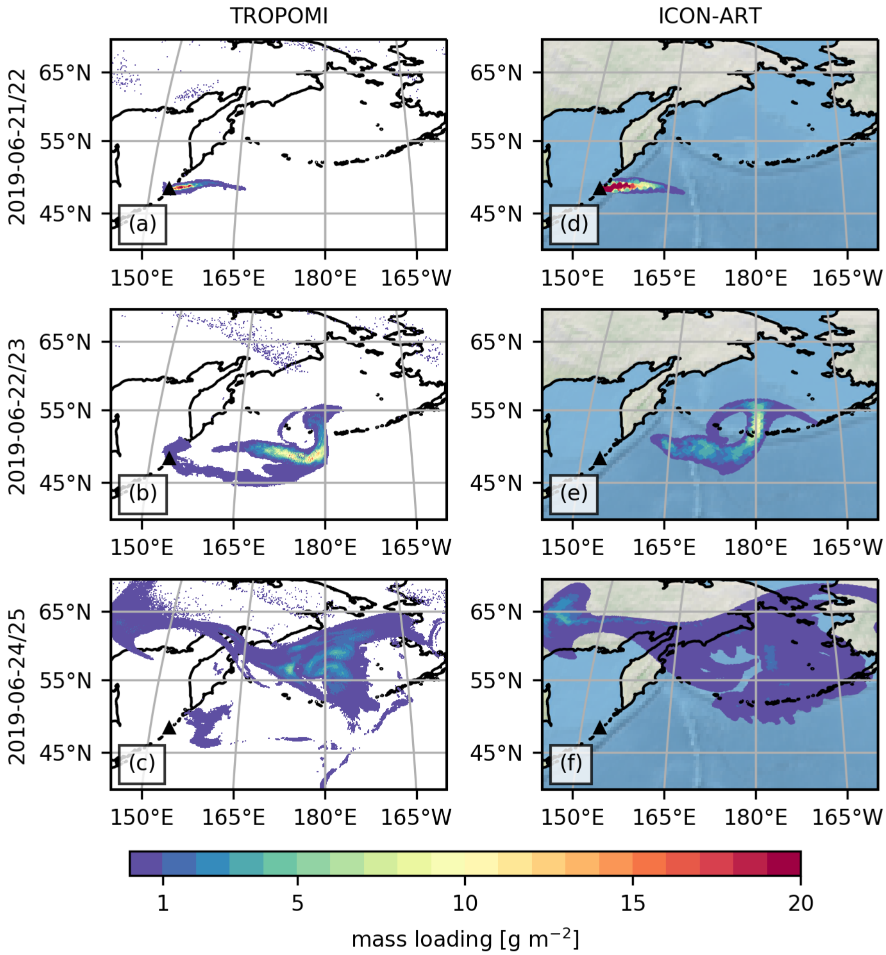

Figure 5. Mass loading of SO_2 measured by TROPOMI during three different time periods are shown in panels (a), (b), and (c). Panels (d), (e), and (f) show ICON-ART results of AERODYN-rad at corresponding time steps.

Figure 5 shows three TROPOMI retrievals of SO_2 mass loading in $\mathrm{g\,m^{-2}}$ in panels (a), (b), and (c) for three different dates. Each of these three graphs is a composite of several satellite orbits, chosen from a batch of 14 consecutive orbits (approximately 24 h coverage). Those orbits that directly detect the volcanic cloud in Fig. 5 (a) intersected with the area of interest (see Sect.

2.1.1) on 22 June 2019, between 02:16 and 02:29 UTC. Data points containing the volcanic cloud signature in Fig. 5 (b) were measured on 23 June, between 00:15 and 02:10 UTC and in Fig. 5 (c) between 24 June, 20:16 UTC and 25 June, 03:13 UTC, respectively. Panels (d) to (f) show ICON-ART results of AERODYN-rad for three different time steps. These time steps have been chosen to be closest to the mean of the time period of the corresponding TROPOMI measurement. The overall structure of the SO_2 mass loading agrees well between model results and observations. This is especially true for the two earlier dates when the modelled atmospheric state can be assumed to be closer to reality than for later dates. But also the model result 3.5 days after its initialization in Fig. 5 (f) shows very good agreement with the TROPOMI measurement in (c). A main difference between satellite retrieval and model result is the location of the maximum SO_2 mass loading. Although the magnitude of the maximum SO_2 mass loading is in good agreement, in the model results its location appears further downstream compared to the satellite measurement. One reason could be the different time of measurement and model result. However, a greater influence can be expected by uncertainties of the emission profile parametrization and of the simulated wind velocities. In case more SO_2 is emitted in altitudes with higher wind speeds in the model, it will be transported faster. The same applies for the case that in some altitudes wind speeds in the model are slightly higher than they are in reality. Furthermore, the TROPOMI measurements can also be erroneous. The TROPOMI sensor might not capture all of the SO_2 due to deficiencies of the measurement technique in opaque regions. Assumptions about a vertical SO_2 profile made for the retrieval can also result in incorrect SO_2 mass loadings.

The AHI and TROPOMI measurements give us confidence in the simulated horizontal distribution of the volcanic cloud. Additionally, we retrieve information about the vertical extension of the volcanic cloud from OMPS-LP and CALIOP data. OMPS-LP gives a clear signal of the volcanic cloud on 22 June 2019, 02:27 UTC shortly after the onset of the eruption. It locates the volcanic cloud at $49.76°$ N $154.1°$ E at approximately 17 km. The ICON-ART model result (AERODYN-rad) shows a similar cloud top height which will be addressed in more detail in Sect. 3.3. Also the height of the volcanic cloud measured by CALIOP on 23 June 2019, agrees well with the model result. This will be addressed in more detail in the following section.

3.2 Effect of aerosol dynamics

So far we ~~only~~ mainly discussed the ICON-ART model result of the AERODYN-rad scenario. In this section, we compare it with the no_AERODYN-rad scenario to study the influence of secondary aerosol formation and particle aging on volcanic aerosol dispersion.

The CALIPSO satellite passed over the volcanic cloud on 23 June 2019, at around 15:00 UTC. On this date, the satellite ground track clearly intersects the modeled volcanic cloud, as shown in Fig. 6 (a). The 2D map depicts the volcanic cloud top height of accumulation mode ash particles calculated with ICON-ART (AERODYN-rad). In this connection, a threshold of 0.01 µg ash per kg air defines the volcanic cloud top. The map shows a maximum volcanic cloud top height in the range of 17–19 km under the CALIPSO ground track at around $50°$ N. The CALIOP measurement for the total attenuated backscatter at 532 nm, shown in Fig. 6 (b), indicates volcanic aerosols between $49°$ N and $51°$ N at height levels between 15 and 16 km. Attenuated backscatter at 532 nm of volcanic aerosols on 23 June for the 15:00 UTC model output (AERODYN-rad) is displayed in Fig. 6 (c). Based on the simulated ash and sulfate concentrations as well as their optical properties the attenuated backscatter is determined for model columns along the CALIPSO ground track.

Our model result (AERODYN-rad) captures the most prominent feature of the CALIOP retrieval between $49°$ N and $51°$ N at a height around 16 km. Here, the model shows a clear maximum in total attenuated backscatter of volcanic aerosol. Furthermore, the model result shows several other peaks in attenuated backscatter. In order to make the model result in panel (c) better comparable with the measurement, the magenta line in panel (b) shows the $0.002\ \mathrm{km}^{-1}\ \mathrm{sr}^{-1}$ contour of the model result. For example, the peak in the simulated attenuated backscatter (Fig. 6 (c)) at around $44°$ N up to 3 km is also present in the CALIOP signal at a comparable order of magnitude. This suggests that the elevated CALIOP signal in this region is due to volcanic aerosols. Other features in the modeled attenuated backscatter, north of $51°$ N, also collocate with structures in the CALIOP signal. This suggests that part of the elevated CALIOP signal in these regions is due to the volcanic aerosol cloud. It nicely shows the advantage of considering model results for the interpretation of satellite retrievals.

Comparing AERODYN-rad in Fig. 6 (c) with no_AERODYN-rad in Fig. 6 (d) shows the distinct effect of aerosol dynamics on vertical distribution of the volcanic cloud. No_AERODYN-rad catches the main feature between $49°$ N and $51°$ N at a height up to 17 km. However, the volcanic aerosol layer extends significantly further north, up to $54°$ N. This is in contrast to the CALIOP signal in Fig. 6 (b). Also the smaller patterns in lower altitudes and higher latitudes are missing in the no_AERODYN-rad scenario. The same applies for the feature at around $44°$ N and 3 km height. Without aerosol dynamics, most of the aerosol stays at one height level, whereas with aerosol dynamics, the particles get also mixed down to lower altitudes. Coagulation of particles and condensation of sulfate and water onto existing particles increases the aerosol mass. Hence, these particles sediment faster and therefore, are removed from the atmosphere more efficiently.

A similar conclusion can be derived from the AERODYN-no_rad and no_AERODYN-no_rad scenarios in Fig. 6 (e) and (f), respectively. Although, both are missing the most prominent feature between $49°$ N and $51°$ N at around 16 km, they show the same behavior in terms of aerosol dynamic effects.

Additional dates of CALIPSO measurements are displayed in Appendix A.

To further investigate the effect of aerosol dynamics on the residence time of very fine ash, we examine the temporal variation of ash concentration in the atmosphere. This is illustrated in Fig. 7. The graph shows how the normalized total ash mass $\widetilde{m}_{ash}$ evolves over time after the onset of the volcanic eruption on 21 June 2019, at 18:00 UTC. We define

$$\widetilde{m}_{ash}(t) = \frac{m_{ash}(t)}{\max(m_{ash}(t))}$$

with $m_{ash}(t)$ as the total observed volcanic ash mass at one measurement time or simulation time step, respectively. In the ICON-ART simulations, AERODYN-rad and no_AERODYN-rad, $\max(m_{ash}(t))$ is close to 1.9×10^9 kg. For the AHI retrieval $\max(m_{ash}(t))$ is estimated to range between 0.4×10^9 and 1.8×10^9 kg. Figure 7 shows $\widetilde{m}_{ash}$ for two different simulation scenarios, AERODYN-rad (green) and no_AERODYN-rad (yellow), and the AHI retrieval (black). The gray shading depicts an error estimate for the AHI measurement between $0.4\widetilde{m}_{ash}$ and $1.6\widetilde{m}_{ash}$.

Both simulations and the satellite measurement agree very well over the course of the first 9 h. This is the eruption phase of the Raikoke volcano. As Raikoke did not erupt continuously over these 9 h, the offset between simulation and observation

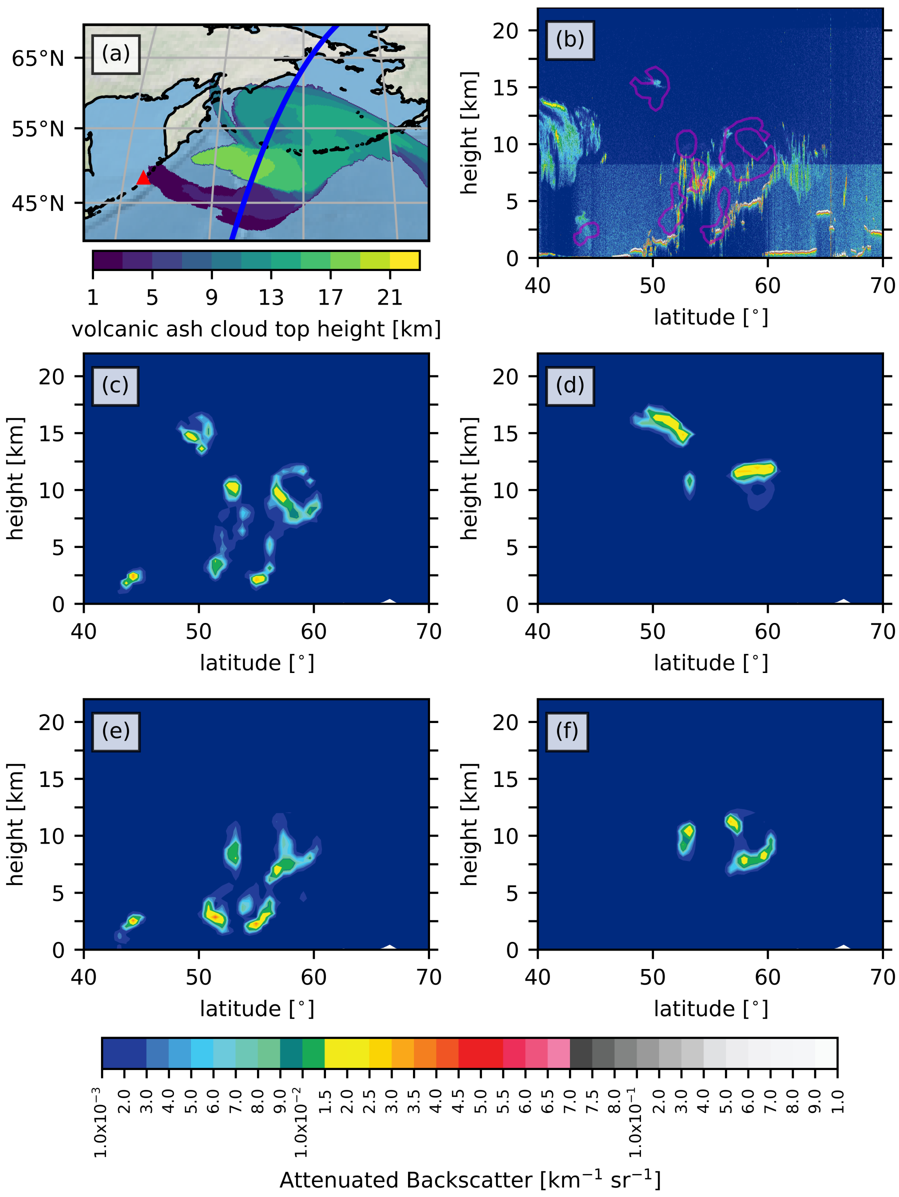

Figure 6. (a) CALIPSO ground track on 23 June 2019, around 15:00 UTC in blue color and location of Raikoke volcano as red triangle. The contour map shows the volcanic ash cloud top height for the AERODYN-rad scenario. (b) The CALIOP attenuated backscatter for 532 nm for the satellite position between 40° N and 70° N is displayed in the top right panel. The magenta line shows the 0.002 $\mathrm{km}^{-1}\,\mathrm{sr}^{-1}$ contour of AERODYN-rad at 15:00 UTC. Middle and lower panels: Total attenuated backscatter for 532 nm of volcanic aerosols under the CALIPSO ground track on 23 June 2019, for the 15:00 UTC model output are displayed. (c) shows the result for AERODYN-rad, (d) for no_AERODYN-rad, (e) for AERODYN-no_rad, and (f) for no_AERODYN-no_rad, respectively.

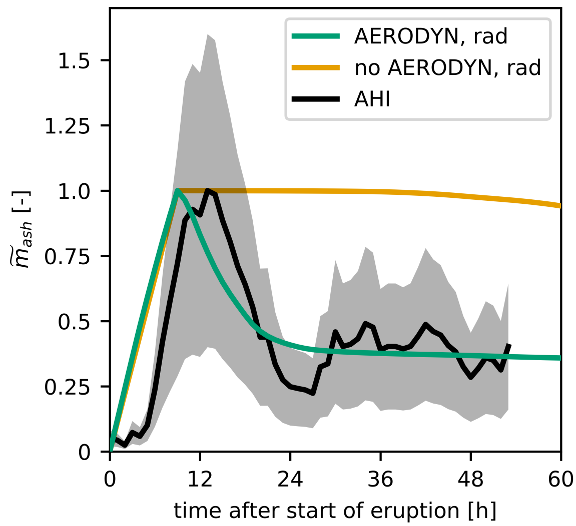

Figure 7. Normalized total volcanic ash mass $\widetilde{m}_{ash}$ over the time after the onset of the volcanic eruption on 21 June 2019, at 18:00 UTC. The green and yellow curve represent AERODYN-rad and no_AERODYN-rad, respectively. The black curve is based on AHI measurements with an error estimate in gray.

as well as the small-scale variations in the observation during this period can be ~~understood~~explained. The main more or less continuous eruption of Raikoke occurred between 21 June 2019, 22:40 UTC and 22 June, 02:00 UTC; with several additional puffs before and after this period. While in the model we assumed a constant and continuous eruption.

After the end of the eruption, the observed ash mass (black) decays to less than $50\,\%$ over the course of $12\ \mathrm{h}$. Thereafter, the total volcanic ash mass seems to stabilize. The small-scale variations in the observation might be due to deficiencies or limitations of the retrieval algorithm, as no new ash is emitted during this period. We can see a very similar ~~behavior~~ decay and stabilization of ash mass for the AERODYN-rad scenario in green. The result suggests that the necessary sink processes are represented by our new aerosol dynamics module. The same are missing in no_AERODYN-rad, for which the volcanic ash mass decays much slower. We deduce that secondary aerosol formation and particle aging, due to condensation and coagulation, are essential processes for the correct simulation of volcanic aerosol dispersion. These processes largely influence the transported aerosol concentrations. Additionally, we would like to note that the prevailing settling mechanism of aerosol after the Raikoke 2019 eruption for all our simulation scenarios is due to sedimentation. Dry deposition is only relevant for aerosol near the ground. Wet deposition should also play a minor role during the first days after the eruption, as most of the volcanic ash is emitted above cloud level.

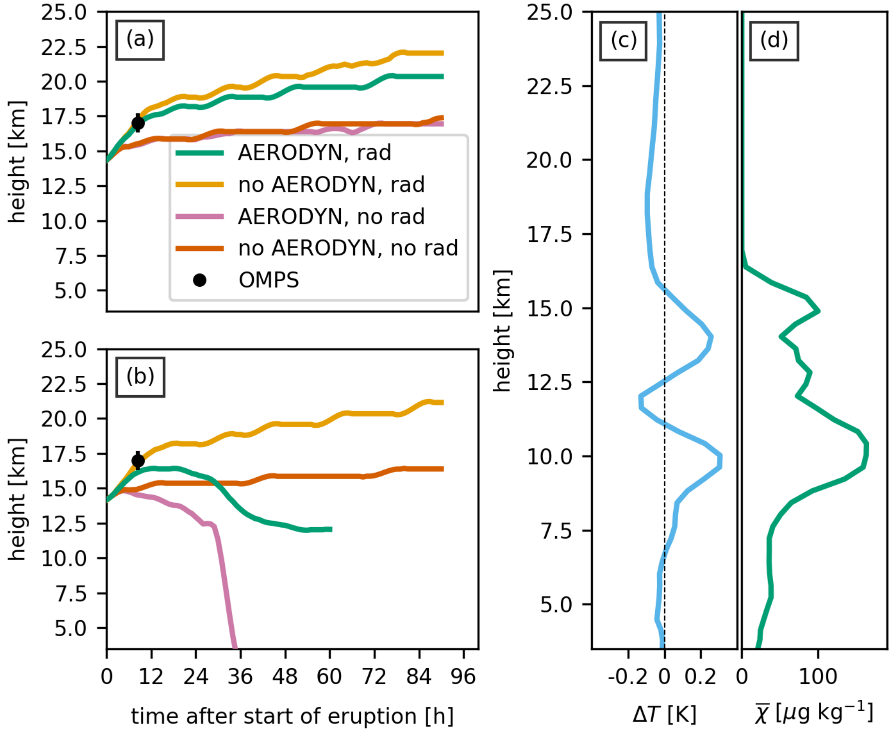

Figure 8. (a) and (b) Evolution of height of volcanic ash cloud top after the onset of the eruption on 21 June 2019, at 18:00 UTC. The yellow curve represents the no_AERODYN-rad scenario, the green curve AERODYN-rad, the pink one AERODYN-no_rad, and the orange one represents the no_AERODYN-no_rad scenario. Panel (a) shows the ash cloud top of particles in the accumulation mode, (b) of particles in the coarse mode, respectively. The black circle depicts the volcanic cloud top height obtained from OMPS-LP. (c) Mean temperature difference (AERODYN-rad – AERODYN-no_rad) in volcanic ash cloud columns on 23 June 2019, 12:00 UTC. (d) Mean volcanic ash concentration $\overline{\chi}$ for the same model columns as in (c) for AERODYN-rad.

3.3 Effect of radiative interaction

In contrast to aerosol dynamics, aerosol–radiation interaction does not largely influence the transported aerosol concentrations. This can be deduced from ~~Fig. 4.~~ the SAL analysis in Table 3. There are only minor differences in the ~~magnitude~~ amplitude of volcanic ash mass loading comparison between the two ~~displayed simulation scenarios (panels (c) to (f))~~scenarios with or without radiation-interaction, but the same aerosol dynamics setup. However, ~~the~~ there are differences in the mass loading patterns that can be explained by radiative effects. This is already somewhat indicated by the S value in Table 3. The S values of simulation scenarios with the same radiation-interaction setup are closer to each other compared to the other scenarios.

In order to investigate the influence of aerosol–radiation interaction on volcanic plume dispersion in more detail, we look at the maximum height that the volcanic cloud reaches over the course of time. A volcanic cloud that is lifted up in the atmosphere has a longer lifetime. Hence, it can be transported over longer distances, remains a hazard for aircraft over a longer period of time, and has longer lasting climatic effects. Additionally, the height of the volcanic cloud in the atmosphere also influences its transport, as wind speed and direction can differ between height levels. Figure 8 (a) and (b) show the height of the volcanic cloud top over the course of time after the onset of the volcanic eruption. We used a threshold value to determine the extent of the volcanic cloud in the model result. A model grid box with an ash concentration above this threshold is considered as part of the volcanic cloud. For accumulation mode ash particles this threshold is set to $0.01\ \mu\mathrm{g\,kg^{-1}}$ and for coarse mode ash particles to ~~0.1~~1 $\mu\mathrm{g\,kg^{-1}}$. The different colours in Fig. 8 (a) and (b) represent the ~~three~~ four different simulated scenarios. The upper panel shows the volcanic cloud top height of ash particles in the accumulation mode. The lower one shows the same graph for ash particles in the coarse mode.

Comparing the yellow (no_AERODYN-rad) with the green curve (AERODYN-rad), we can see the influence of the aerosol dynamic processes on the maximum volcanic cloud top height. For both, the accumulation and the coarse mode the volcanic cloud top height is lower for the scenario with AERODYN. This result agrees with the backscatter signal of the same two simulation scenarios in Fig. 6. Due to aerosol dynamic processes particles grow in size as they age over time. Hence, the volcanic cloud is located at lower altitudes. This effect is more pronounced for the larger and therefore heavier coarse mode particles. Due to their larger surface, the condensation of sulfate onto them is more efficient compared to accumulation mode particles. The result indicates that for coarse mode ash the aging process is the determining factor of whether the volcanic cloud rises higher or sinks. The ash cloud top height of coarse mode ash particles in no_AERODYN-rad continuously rises up to more than $20\ \mathrm{km}$. In contrast, the ash cloud top height in AERODYN-rad gradually sinks during the following $50\ \mathrm{h}$ (after reaching its peak). The graph for the AERODYN-rad scenario ~~starts fluctuating after around 50~~stops after around $60\ \mathrm{h}$~~and should be left out of the discussion~~. This behaviour can be explained by the evaluation method. The aged coarse mode particles sediment out and reduce their concentration significantly. Eventually, the concentration sinks to the same order of the threshold value that is used to determine the volcanic cloud. From this point onward, the maximum volcanic cloud top height cannot be determined reliably anymore.

Even more pronounced than the aerosol dynamic effect, we can see the influence of radiative effects on the volcanic cloud dispersion in Fig. 8. A distinct difference prevails between the two scenarios with radiative interaction (yellow and green curve) and the ~~one~~ two without radiative interaction (pink and orange curve). Accumulation mode ash particles stay more or less at the initial maximum height level ($14\ \mathrm{km}$) in case they do not interact with radiation. On the contrary, the ash cloud top rises up to $20\ \mathrm{km}$ in the two scenarios with radiative interaction over the first four days after the onset of the eruption. Furthermore, the graph for accumulation mode ash particles indicates that the aerosol aging reduces the lifting effect induced by radiative interaction by higher sedimentation velocities due to larger particles. Hence, pure ash particles are lifted higher compared to aged ash particles.

The described behavior is even more pronounced for coarse mode ash particles, shown in Fig. 8 (b). Especially for the simulated scenario with no radiative interaction, but aerosol dynamic processes (pink curve), the ash particles sediment out over the course of the first $30\ \mathrm{h}$ after the onset of the eruption. In contrast, the two scenarios with radiative interaction again show a lifting in volcanic cloud top height over the first $12\ \mathrm{h}$. Subsequently, the influence of particle aging becomes more relevant for coarse mode ash particles. As for accumulation mode particles, in the no_AERODYN-no_rad scenario (orange curve) coarse mode particles also tend to stay on the same height level.

A direct effect of the radiative interaction is shown in Fig. 8 (c) and (d) exemplarily for the model result of 23 June 2019, 12:00 UTC. The graph in (c) depicts the horizontally averaged atmospheric temperature difference ΔT between AERODYN-rad and AERODYN-no_rad at different heights. For the averaging approach, only model columns which contain a volcanic ash mass loading $> 0.01\ \mathrm{g\,m^{-2}}$ in both scenarios are considered. Figure 8 (d) illustrates the horizontally averaged volcanic ash concentration $\overline{\chi}$ at different heights for the AERODYN-rad scenario. For this averaging we consider exactly the same model columns as we use for the temperature difference. The curve of the temperature difference shows two distinct peaks, one at around 10 the other at around $14\ \mathrm{km}$. Here, the simulation which considers aerosol–radiation interaction exhibits around $0.25\ \mathrm{K}$ higher air temperature. Both peaks collocate with the lower and upper boundary of the volcanic ash cloud, respectively. In these two height layers, the volcanic ash leads to an increased absorption of solar and thermal radiation, hence, it heats the surrounding air. The resulting vertical velocity perturbation Δw is in the order of $0.1\ \mathrm{ms^{-1}}$. For this purpose, we analyzed the difference in vertical velocity between the AERODYN-rad and AERODYN-no_rad scenario during the first $12\ \mathrm{h}$ after the eruption. Only grid cells in model columns which contain a volcanic ash mass loading $> 0.01\ \mathrm{g\,m^{-2}}$ in both scenarios are considered. Locally, Δw reaches $0.19\ \mathrm{ms^{-1}}$ with a 98th percentile of $0.05\ \mathrm{ms^{-1}}$. This agrees well with the vertical lifting of the volcanic cloud top height of around $3\ \mathrm{km}$ during the first $12\ \mathrm{h}$ ($\overline{w} = 0.07\ \mathrm{ms^{-1}}$).

The comparison of the ~~three~~ four simulated scenarios with the OMPS-LP retrieval indicates that considering aerosol radiative effects is essential to simulate volcanic aerosol dispersion correctly, already over the course of the first four days after the start of the eruption. Especially the simulated height of the accumulation mode particle's cloud top in Fig. 8 (a) agrees very well with the measured height. It should be noted that the OMPS-LP measurement gives the volcanic cloud height at one (horizontal) position. The maximum volcanic cloud top height is not necessarily collocated with this measurement position. However, at this early stage during the eruption phase the volcanic cloud is not distributed over a large area yet. That is why we assume that the volcanic cloud top height does not differ significantly in horizontal direction. Additionally, the ICON-ART model result shows the maximum volcanic cloud top height in proximity to the location of the satellite measurement. Based on the simulation result, we assume that mainly accumulation mode particles are present at the top of the volcanic cloud. These particles are in the size of $0.1\ \mathrm{\mu m}$.

4 Conclusions

In the scope of this work, we use the Raikoke eruption of June 2019 as a natural experiment to investigate the influence of particle aging and aerosol–radiation interaction on volcanic aerosol dispersion. We simulate volcanic aerosol dispersion with the ICON-ART modelling system together with the newly implemented AERODYN module. The results presented allow us to answer the posed research questions:

1) Particle aging generates internally mixed aerosols due to condensation and coagulation. These processes generally increase particle sizes and consequently, the sedimentation velocity. Therefore, ash aging mainly influences the sink processes.

As a consequence of the higher sedimentation velocity, also the vertical distribution of volcanic aerosols is affected. Our results suggest that aerosol dynamic effects lead to a removal of around $50\,\%$ of volcanic ash mass (very fine ash) over the course of $12\,\mathrm{h}$ after the end of the Raikoke eruption on 22 June 2019.

2) The aerosol–radiation interaction has a significant impact on the volcanic aerosol dispersion already during the very first days after the eruption. Without this interaction volcanic ash sediments out fast and does not reach height levels measured by satellite instruments, such as OMPS-LP. Our results suggest that the Raikoke volcanic cloud top rises around $3\,\mathrm{km}$ during the first $12\,\mathrm{h}$ and reaches a height of more than $20\,\mathrm{km}$ after 4 days.

3) The comparison between model results and satellite retrievals, such as CALIOP and AHI, suggests that aerosol dynamic processes are crucial for the correct simulation of volcanic aerosol dispersion during the first couple of days after the eruption. Both, the aging process and the aerosol–radiation interaction influence the vertical distribution of aerosols and therefore, determine at which altitude the particles are transported. The radiative effect is responsible for the rise of the volcanic cloud top, whereas the particle aging is responsible for an efficient mixing of aerosols into lower altitudes. Furthermore, this study illustrates that representing sink processes correctly is necessary for the correct and reliable forecast of volcanic aerosol dispersion.

Code and data availability. The output from ICON-ART simulations performed in this study ~~will be made available on KIT-Open data archive~~can be provided upon request by the corresponding author . The ICON-ART code is licence protected and can be accessed by request to the corresponding author. The NOAA Ash Height Product (Pavolonis, Michael, Qi, Hongming, and NOAA JPSS Program Office (2017): NOAA JPSS Visible Infrared Imaging Radiometer Suite (VIIRS) Volcanic Ash Detection and Height Environmental Data Record (EDR) from NDE. NOAA National Centers for Environmental Information. doi:10.7289/V5BK19KS. [Accessed in April 2020]) is available from the NOAA Comprehensive Large Array-data Stewardship System (CLASS) archive (http://www.class.noaa.gov/saa/products/search?datatype_family=JPSS_GRAN). The MODIS Cloud Product (Platnick, S., S. Ackerman, M. King, G. Wind, K. Meyer, P. Menzel, R. Frey, R. Holz, B. Baum, and P. Yang, 2017. MODIS atmosphere L2 cloud product (06_L2), NASA MODIS Adaptive Processing System, Goddard Space Flight Center, [doi:10.5067/MODIS/MOD06_L2.061; doi:10.5067/MODIS/MYD06_L2.061]) and the SNPP VIIRS Cloud Properties product (doi:10.5067/VIIRS/CLDPROP_L2_VIIRS_SNPP.011) are available from the NASA LAADS DAAC (https://ladsweb.modaps.eosdis.nasa.gov). TROPOMI data is publicly available on https://s5phub.copernicus.eu. Himawari-8 AHI datasets that have been analyzed in the scope of this study ~~will be made available on KIT-Open data archive~~can be provided upon request by the corresponding author . OMPS data is available after registration at https://www.iup.uni-bremen.de/DataRequest/. CALIPSO data can be found on https://eosweb.larc.nasa.gov/project/calipso/calipso_table/.

Appendix A: Total Attenuated Backscatter at 532 nm

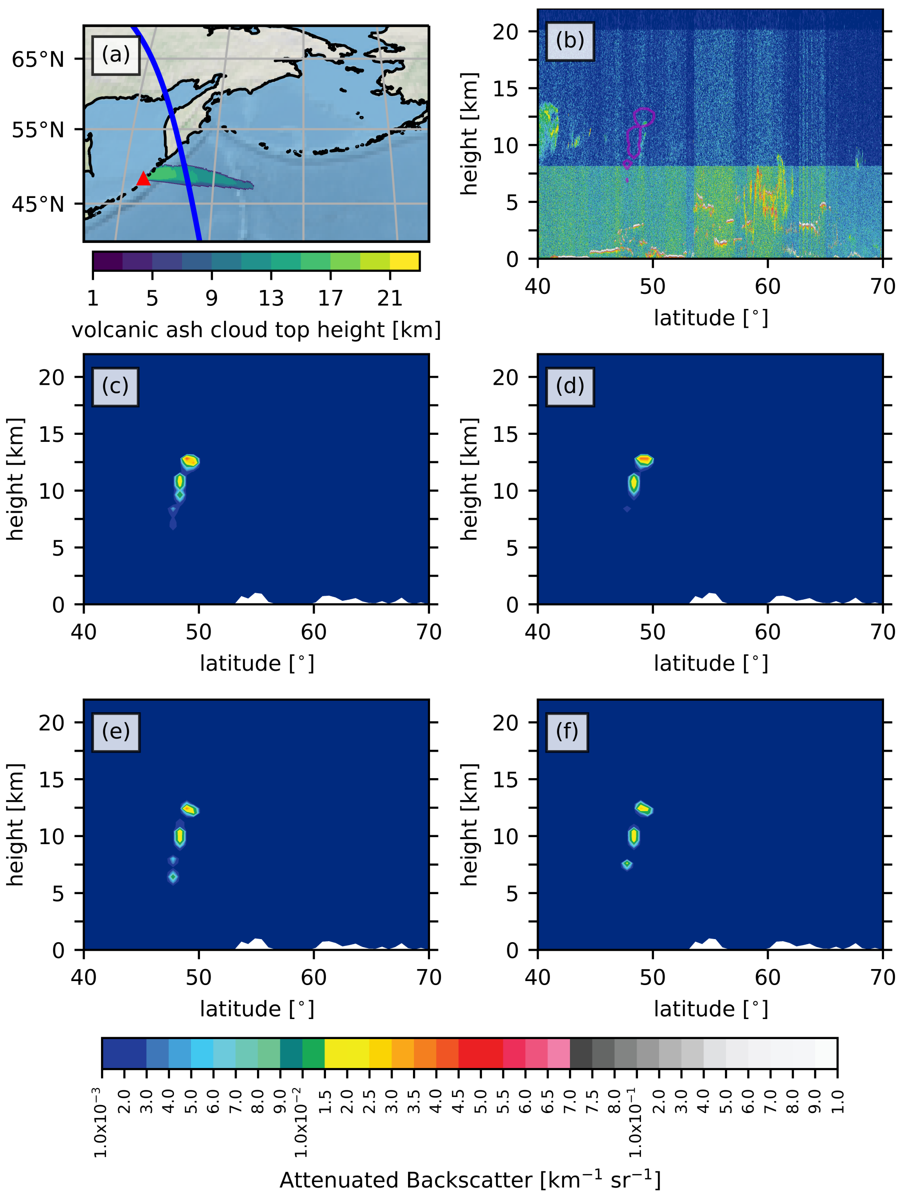

Figure A1. (a) CALIPSO ground track on 22 June 2019, around 03:00 UTC in blue color and location of Raikoke volcano as red triangle. The contour map shows the volcanic ash cloud top height for the AERODYN-rad scenario. (b) The CALIOP attenuated backscatter for 532 nm for the satellite position between 40° N and 70° N is displayed in the top right panel. The magenta line shows the 0.002 km^{-1} sr^{-1} contour of AERODYN-rad at 03:00 UTC. Middle and lower panels: Total attenuated backscatter for 532 nm of volcanic aerosols under the CALIPSO ground track on 22 June 2019, for the 03:00 UTC model output are displayed. (c) shows the result for AERODYN-rad, (d) for no_AERODYN-rad, (e) for AERODYN-no_rad, and (f) for no_AERODYN-no_rad, respectively.

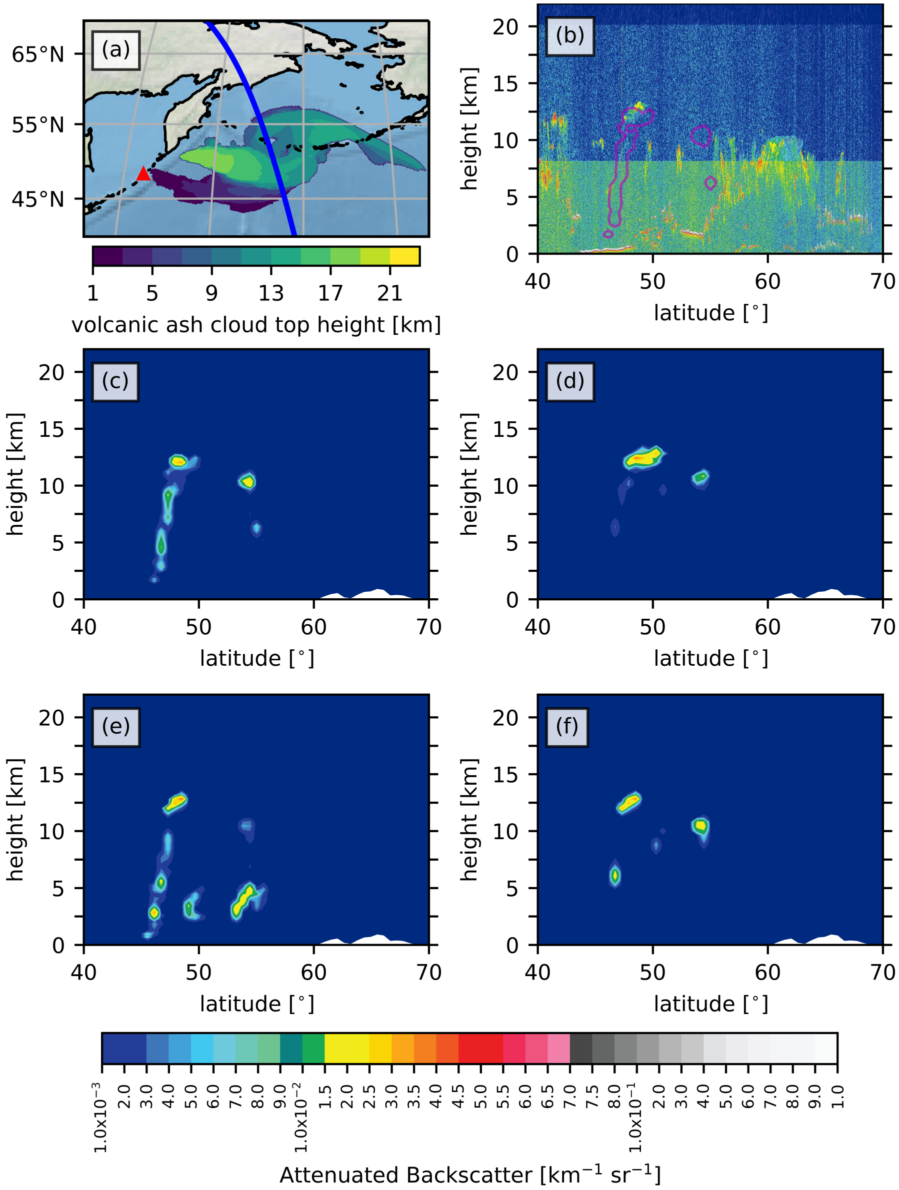

Figure A2. Same as Fig. A1 on 23 June 2019, 02:00 UTC.

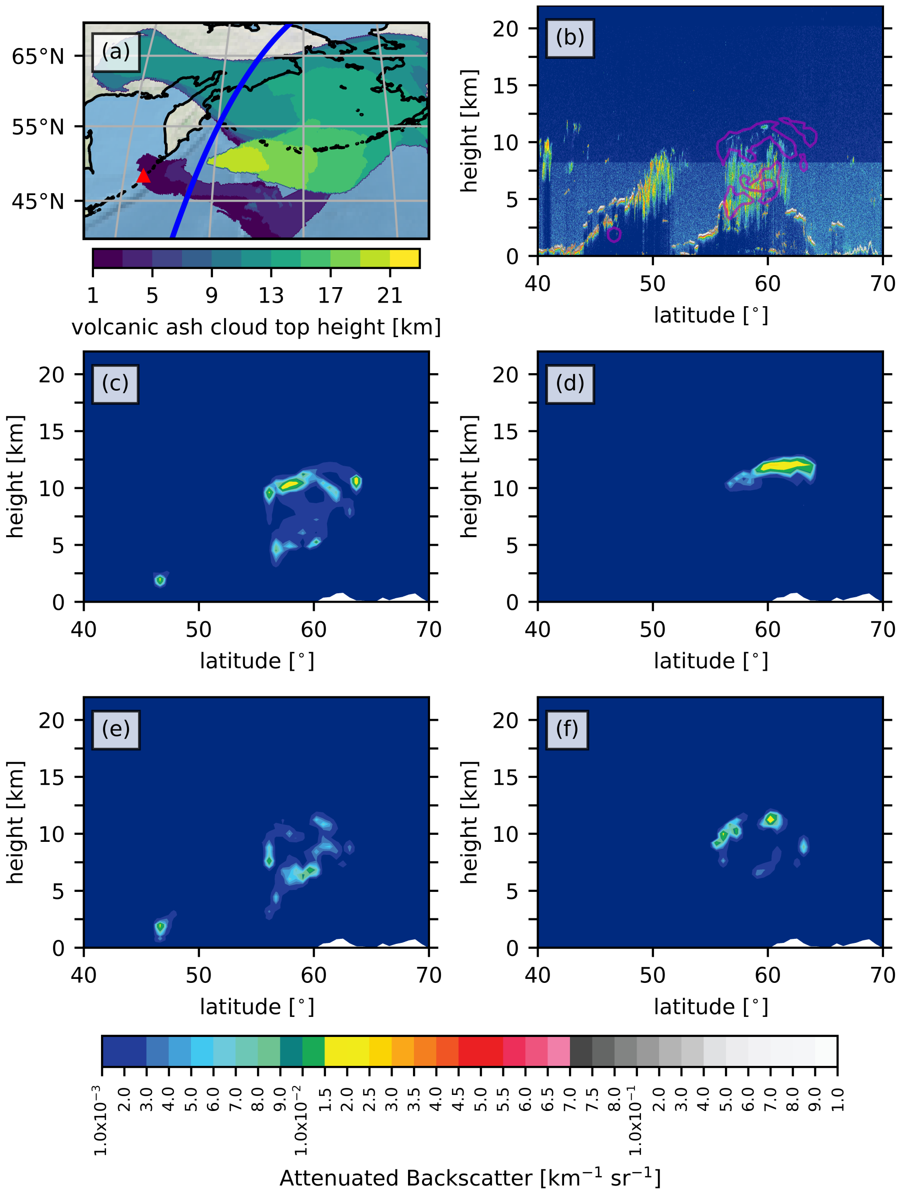

Figure A3. Same as Fig. A1 on 24 June 2019, 16:00 UTC.

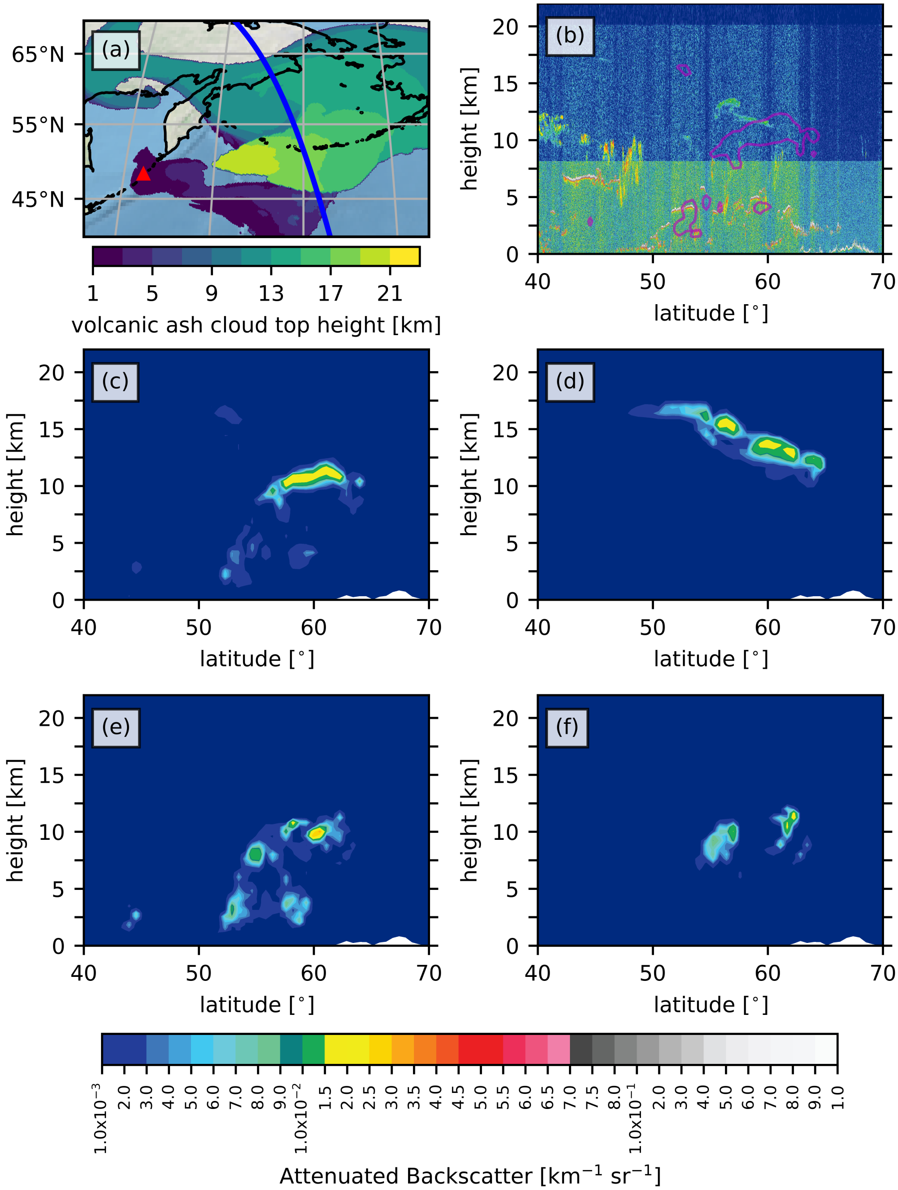

Figure A4. Same as Fig. A1 on 25 June 2019, 01:00 UTC.

525 *Author contributions.* LOM, GAH, HV, JB and BV developed the ICON-ART AERODYN code and carried out the simulations. GAH and JB conducted and analyzed 1D plume simulations. AH provided the plume height estimates based on MODIS and VIIRS data. SPW contributed the TROPOMI analysis. EM and AR provided data from OMPS-LP. CvS provided CALIOP data. FJP retrieved and analyzed AHI data. LOM and GAH prepared the manuscript with significant contributions from all authors.

Competing interests. The authors declare that they have no conflict of interest.

Acknowledgements. The main contribution to this work by LOM has been funded under FE-Nr. 50.0368/2017 by BMVI (Federal Ministry of Transport and Digital Infrastructure of Germany). The contributions from GAH, AH, and JB are within the VolPlume project as a part of the research unit VolImpact funded by German research foundation DFG (FOR 2820). As part of the same research unit (VolImpact), EM, AR, and CvS contributed within the VolARC project and S~~P~~W within VolDyn, respectively.

References

Abdelkader, M., Metzger, S., Steil, B., Klingmüller, K., Tost, H., Pozzer, A., Stenchikov, G., Barrie, L., and Lelieveld, J.: Sensitivity of transatlantic dust transport to chemical aging and related atmospheric processes, Atmos. Chem. Phys., 17, 3799–3821, https://doi.org/10.5194/acp-17-3799-2017, https://www.atmos-chem-phys.net/17/3799/2017/, 2017.

Ayris, P. M. and Delmelle, P.: Volcanic and atmospheric controls on ash iron solubility: A review, Phys. Chem. Earth, 45-46, 103–112, https://doi.org/10.1016/j.pce.2011.04.013, http://dx.doi.org/10.1016/j.pce.2011.04.013, 2012.

Bagheri, G. and Bonadonna, C.: Aerodynamics of Volcanic Particles: Characterization of Size, Shape, and Settling Velocity, in: Volcanic Ash Hazard Observation, edited by MACKIE, S., CASHMAN, K., RICKETTS, H., RUST, A., and WATSON, M., Elsevier, 2016.

Bagnato, E., Aiuppa, A., Bertagnini, A., Bonadonna, C., Cioni, R., Pistolesi, M., Pedone, M., and Hoskuldsson, A.: Scavenging of sulphur, halogens and trace metals by volcanic ash: The 2010 Eyjafjallajökull eruption, Geochim. Cosmochim. Ac., 103, 138–160, https://doi.org/10.1016/j.gca.2012.10.048, http://dx.doi.org/10.1016/j.gca.2012.10.048, 2013.

Bohren, C. F. and Huffman, D. R.: Absorption and Scattering of Light by Small Particles, Wiley New York, 1983.

Bonadonna, C. and Scollo, S.: IAVCEI Commission on Tephra Hazard Modelling, http://www.ct.ingv.it/iavcei/results.htm, last access: 03 September 2020, 2013.

Bond, T. C., Habib, G., and Bergstrom, R. W.: Limitations in the enhancement of visible light absorption due to mixing state, J. Geophys. Res.-Atmos., 111, https://doi.org/10.1029/2006JD007315, 2006.

Brown, R. J., Bonadonna, C., and Durant, A. J.: A review of volcanic ash aggregation, Phys. Chem. Earth, 45-46, 65–78, https://doi.org/10.1016/j.pce.2011.11.001, http://dx.doi.org/10.1016/j.pce.2011.11.001, 2012.

Casadevall, T. J.: Volcanic ash and aviation safety: Proceedings of the first international symposium on volcanic ash and aviation safety, Tech. rep., US Geological Survey, https://doi.org/10.3133/b2047, https://pubs.er.usgs.gov/publication/b2047, 1994.

Clarisse, L. and Prata, F.: Infrared sounding of volcanic ash, in: Volcanic Ash, pp. 189–215, Elsevier, 2016.

Clarisse, L., Hurtmans, D., Prata, A. J., Karagulian, F., Clerbaux, C., De Mazière, M., and Coheur, P.-F.: Retrieving radius, concentration, optical depth, and mass of different types of aerosols from high-resolution infrared nadir spectra, Appl. Optics, 49, 3713–3722, 2010.

Dee, D. P., Uppala, S. M., Simmons, A. J., Berrisford, P., Poli, P., Kobayashi, S., Andrae, U., Balmaseda, M. A., Balsamo, G., Bauer, P., Bechtold, P., Beljaars, A. C. M., van de Berg, L., Bidlot, J., Bormann, N., Delsol, C., Dragani, R., Fuentes, M., Geer, A. J., Haimberger, L., Healy, S. B., Hersbach, H., Hólm, E. V., Isaksen, L., Kållberg, P., Köhler, M., Matricardi, M., McNally, A. P., Monge-Sanz, B. M., Morcrette, J.-J., Park, B.-K., Peubey, C., de Rosnay, P., Tavolato, C., Thépaut, J.-N., and Vitart, F.: The ERA-Interim reanalysis: configuration and performance of the data assimilation system, Quart. J. Roy. Meteorol. Soc., 137, 553–597, https://doi.org/10.1002/qj.828, https://rmets.onlinelibrary.wiley.com/doi/abs/10.1002/qj.828, 2011.

Delmelle, P., Lambert, M., Dufrêne, Y., Gerin, P., and Óskarsson, N.: Gas/aerosol-ash interaction in volcanic plumes: New insights from surface analyses of fine ash particles, Earth Planet Sc. Lett., https://doi.org/10.1016/j.epsl.2007.04.052, 2007.

Durant, A. J., Bonadonna, C., and Horwell, C. J.: Atmospheric and environmental impacts of volcanic particulates, Elements, 6, 235–240, https://doi.org/10.2113/gselements.6.4.235, 2010.

Folch, A., Costa, A., and Macedonio, G.: FPLUME-1.0: An integral volcanic plume model accounting for ash aggregation, Geosci. Model. Dev., 9, 431–450, https://doi.org/10.5194/gmd-9-431-2016, 2016.

Fountoukis, C. and Nenes, A.: ISORROPIA II: a computationally efficient thermodynamic equilibrium model for K +-Ca 2+-Mg 2+-NH + 4-Na +-SO 2- 4-NO - 3-Cl –H 2 O aerosols, Atmos. Chem. Phys., 7, 4639–4659, www.atmos-chem-phys.net/7/4639/2007/, 2007.

Gasch, P., Rieger, D., Walter, C., Khain, P., Levi, Y., Knippertz, P., and Vogel, B.: Revealing the meteorological drivers of the September 2015 severe dust event in the Eastern Mediterranean, Atmos. Chem. Phys., 17, 13 573–13 604, https://doi.org/10.5194/acp-17-13573-2017, 2017.

Gasteiger, J., Grobß, S., Freudenthaler, V., Wiegner, M., Groß, S., Freudenthaler, V., and Wiegner, M.: Volcanic ash from Iceland over Munich: mass concentration retrieved from ground-based remote sensing measurements, Atmos. Chem. Phys., 11, 2209–2223, https://doi.org/10.5194/acp-11-2209-2011, 2011.

Giorgetta, M. A., Brokopf, R., Crueger, T., Esch, M., Fiedler, S., Helmert, J., Hohenegger, C., Kornblueh, L., Köhler, M., Manzini, E., Mauritsen, T., Nam, C., Raddatz, T., Rast, S., Reinert, D., Sakradzija, M., Schmidt, H., Schneck, R., Schnur, R., Silvers, L., Wan, H., Zängl, G., and Stevens, B.: ICON-A, the Atmosphere Component of the ICON Earth System Model: I. Model Description, J. Adv. Model. Earth Sy., 10, 1613–1637, https://doi.org/10.1029/2017MS001242, https://agupubs.onlinelibrary.wiley.com/doi/abs/10.1029/2017MS001242, 2018.

Gordon, I. E., Rothman, L. S., Hill, C., Kochanov, R. V., Tan, Y., Bernath, P. F., Birk, M., Boudon, V., Campargue, A., Chance, K. V., Drouin, B. J., Flaud, J. M., Gamache, R. R., Hodges, J. T., Jacquemart, D., Perevalov, V. I., Perrin, A., Shine, K. P., Smith, M. A., Tennyson, J., Toon, G. C., Tran, H., Tyuterev, V. G., Barbe, A., Császár, A. G., Devi, V. M., Furtenbacher, T., Harrison, J. J., Hartmann, J. M., Jolly, A., Johnson, T. J., Karman, T., Kleiner, I., Kyuberis, A. A., Loos, J., Lyulin, O. M., Massie, S. T., Mikhailenko, S. N., Moazzen-Ahmadi, N., Müller, H. S., Naumenko, O. V., Nikitin, A. V., Polyansky, O. L., Rey, M., Rotger, M., Sharpe, S. W., Sung, K., Starikova, E., Tashkun, S. A., Auwera, J. V., Wagner, G., Wilzewski, J., Wcisło, P., Yu, S., and Zak, E. J.: The HITRAN2016 molecular spectroscopic database, J. Quant. Spectrosc. Ra., 203, 3–69, https://doi.org/10.1016/j.jqsrt.2017.06.038, 2017.

Gouhier, M., Eychenne, J., Azzaoui, N., Guillin, A., Deslandes, M., Poret, M., Costa, A., and Husson, P.: Low efficiency of large volcanic eruptions in transporting very fine ash into the atmosphere, Sci. Rep.-UK, 9, 1–12, https://doi.org/10.1038/s41598-019-38595-7, 2019.

Guffanti, M., Casadevall, T., and Budding, K.: Encounters of aircraft with volcanic ash clouds: A compilation of known incidents, 1953-2009, U.S. Geological Survey Data Series 545, 1.0, 12, http://pubs.usgs.gov/ds/545, 2010.

Harvey, N. J., Huntley, N., Dacre, H. F., Goldstein, M., Thomson, D., and Webster, H.: Multi-level emulation of a volcanic ash transport and dispersion model to quantify sensitivity to uncertain parameters, Nat. Hazard. Earth Sys., 18, 41–63, https://doi.org/10.5194/nhess-18-41-2018, https://www.nat-hazards-earth-syst-sci.net/18/41/2018/, 2018.

Heidinger, A. and Li, Y.: Enterprise AWG Cloud Height Algorithm (ACHA) - Algorithm Theoretical Basis Document, Tech. rep., NOAA NESDIS CENTER for SATELLITE APPLICATIONS and RESEARCH, https://docs.google.com/document/d/1m2SatR91WIJcaAZweongcFCb6Wsx_xnRUcZxp94gXHk, 2019.

Heinze, R., Dipankar, A., Henken, C. C., Moseley, C., Sourdeval, O., Trömel, S., Xie, X., Adamidis, P., Ament, F., Baars, H., Barthlott, C., Behrendt, A., Blahak, U., Bley, S., Brdar, S., Brueck, M., Crewell, S., Deneke, H., Di Girolamo, P., Evaristo, R., Fischer, J., Frank, C., Friederichs, P., Göcke, T., Gorges, K., Hande, L., Hanke, M., Hansen, A., Hege, H.-C., Hoose, C., Jahns, T., Kalthoff, N., Klocke, D., Kneifel, S., Knippertz, P., Kuhn, A., van Laar, T., Macke, A., Maurer, V., Mayer, B., Meyer, C. I., Muppa, S. K., Neggers, R. A. J., Orlandi, E., Pantillon, F., Pospichal, B., Röber, N., Scheck, L., Seifert, A., Seifert, P., Senf, F., Siligam, P., Simmer, C., Steinke, S., Stevens, B., Wapler, K., Weniger, M., Wulfmeyer, V., Zängl, G., Zhang, D., and Quaas, J.: Large-eddy simulations over Germany using ICON: a comprehensive evaluation, Quart. J. Roy. Meteorol. Soc., 143, 69–100, https://doi.org/10.1002/qj.2947, https://rmets.onlinelibrary.wiley.com/doi/abs/10.1002/qj.2947, 2017.

Hoshyaripour, G. a., Hort, M., and Langmann, B.: Ash iron mobilization through physicochemical processing in volcanic eruption plumes: a numerical modeling approach, Atmos. Chem. Phys., 15, 9361–9379, https://doi.org/10.5194/acp-15-9361-2015, http://www.atmos-chem-phys.net/15/9361/2015/, 2015.

Hoshyaripour, G. A., Bachmann, V., Förstner, J., Steiner, A., Vogel, H., Wagner, F., Walter, C., and Vogel, B.: Effects of Particle Non-Sphericity on Dust Optical Properties in a Forecast System: Implications for Model-Observation Comparison, J. Geophys. Res.-Atmos., https://doi.org/10.1029/2018JD030228, http://doi.wiley.com/10.1029/2018JD030228, 2019.

Jacobson, M. Z.: A physically-based treatment of elemental carbon optics: Implications for global direct forcing of aerosols, Geophys. Res. Lett., 27, 217–220, https://doi.org/10.1029/1999GL010968, 2000.

Kaiser, J. C., Hendricks, J., Righi, M., Riemer, N., Zaveri, R. A., Metzger, S., and Aquila, V.: The MESSy aerosol submodel MADE3 (v2.0b): Description and a box model test, Geosci. Model. Dev., 7, 1137–1157, https://doi.org/10.5194/gmd-7-1137-2014, 2014.

Khaykin, S. M., Godin-Beekmann, S., Keckhut, P., Hauchecorne, A., Jumelet, J., Vernier, J.-P., Bourassa, A., Degenstein, D. A., Rieger, L. A., Bingen, C., Vanhellemont, F., Robert, C., DeLand, M., and Bhartia, P. K.: Variability and evolution of the midlatitude stratospheric aerosol budget from 22 years of ground-based lidar and satellite observations, Atmos. Chem. Phys., 17, 1829–1845, https://doi.org/10.5194/acp-17-1829-2017, https://www.atmos-chem-phys.net/17/1829/2017/, 2017.

Mackie, S. and Watson, M.: Probabilistic detection of volcanic ash using a Bayesian approach, J. Geophys. Res.-Atmos., 119, 2409–2428, 2014.

Malinina, E.: Retrieval of stratospheric aerosol characteristics from spaceborne limb sounders, PhD Thesis, University of Bremen, http://nbn-resolving.de/urn:nbn:de:gbv:46-00107153-12, 2019.

Malinina, E., Rozanov, A., Niemeier, U., Peglow, S., Arosio, C., Wrana, F., Timmreck, C., von Savigny, C., and Burrows, J. P.: Changes in stratospheric aerosol extinction coefficient after the 2018 Ambae eruption as seen by OMPS-LP and ECHAM5-HAM, Atmospheric Chemistry and Physics Discussions, 2020, 1–25, https://doi.org/10.5194/acp-2020-749, https://acp.copernicus.org/preprints/acp-2020-749/, 2020.

Marti, A., Folch, A., Jorba, O., and Janjic, Z.: Volcanic ash modeling with the online NMMB-MONARCH-ASH v1.0 model: model description, case simulation, and evaluation, Atmos. Chem. Phys., 17, 4005–4030, https://doi.org/10.5194/acp-17-4005-2017, https://www.atmos-chem-phys.net/17/4005/2017/, 2017.

Mastin, L., Guffanti, M., Servranckx, R., Webley, P., Barsotti, S., Dean, K., Durant, A., Ewert, J., Neri, A., Rose, W., Schneider, D., Siebert, L., Stunder, B., Swanson, G., Tupper, A., Volentik, A., and Waythomas, C.: A multidisciplinary effort to assign realistic source parameters to models of volcanic ash-cloud transport and dispersion during eruptions, J. Volcanol. Geoth. Res., 186, 10–21, https://doi.org/10.1016/j.jvolgeores.2009.01.008, 2009.

Mastin, L. G.: A user-friendly one-dimensional model for wet volcanic plumes, Geochem. Geophy. Geosy., 8, https://doi.org/10.1029/2006GC001455, 2007.

Mather, T. A.: Volcanism and the atmosphere: the potential role of the atmosphere in unlocking the reactivity of volcanic emissions., Philosophical transactions. Series A, Mathematical, physical, and engineering sciences, 366, 4581–4595, https://doi.org/10.1098/rsta.2008.0152, 2008.

Mätzler, C.: MATLAB Functions for Mie Scattering and Absorption, Tech. rep., University of Bern, 2002.

Menzel, W., Frey, R., and Baum, B.: Cloud Top Properties and Cloud Phase - Algorithm Theoretical Basis Document, Tech. rep., University of Wisconsin - Madison, https://atmosphere-imager.gsfc.nasa.gov/sites/default/files/ModAtmo/MOD06-ATBD_2015_05_01_1.pdf, 2015.

Mlawer, E. J., Taubman, S. J., Brown, P. D., Iacono, M. J., and Clough, S. A.: Radiative transfer for inhomogeneous atmospheres: RRTM, a validated correlated-k model for the longwave, J. Geophys. Res.-Atmos., 102, 16 663–16 682, https://doi.org/10.1029/97jd00237, 1997.

Niemeier, U., Timmreck, C., Graf, H.-F., Kinne, S., Rast, S., and Self, S.: Initial fate of fine ash and sulfur from large volcanic eruptions, Atmos. Chem. Phys., 9, 9043–9057, https://doi.org/10.5194/acp-9-9043-2009, https://www.atmos-chem-phys.net/9/9043/2009/, 2009.

Pavolonis, M. J., Heidinger, A. K., and Sieglaff, J.: Automated retrievals of volcanic ash and dust cloud properties from upwelling infrared measurements, J. Geophys. Res.-Atmos., 118, 1436–1458, https://doi.org/10.1002/jgrd.50173, https://agupubs.onlinelibrary.wiley.com/doi/abs/10.1002/jgrd.50173, 2013.

Peterson, P. K., Pöhler, D., Sihler, H., Zielcke, J., General, S., Frieß, U., Platt, U., Simpson, W. R., Nghiem, S. V., Shepson, P. B., Stirm, B. H., Dhaniyala, S., Wagner, T., Caulton, D. R., Fuentes, J. D., and Pratt, K. A.: Observations of bromine monoxide transport in the Arctic sustained on aerosol particles, Atmos. Chem. Phys., 17, 7567–7579, https://doi.org/10.5194/acp-17-7567-2017, https://www.atmos-chem-phys.net/17/7567/2017/, 2017.

Prata, A.: Infrared radiative transfer calculations for volcanic ash clouds, Geophys. Res. Lett., 16, 1293–1296, 1989.

Prata, A. and Prata, A.: Eyjafjallajökull volcanic ash concentrations determined using Spin Enhanced Visible and Infrared Imager measurements, J. Geophys. Res.-Atmos. (1984–2012), 117, 2012.

Prata, A., O Brien, D., Rose, W., and Self, S.: Global, long-term sulphur dioxide measurements from TOVS data: A new tool for studying explosive volcanism and climate, GEOPHYSICAL MONOGRAPH-AMERICAN GEOPHYSICAL UNION, 139, 75–92, 2003.

Prata, A. T., Dacre, H. F., Irvine, E. A., Mathieu, E., Shine, K. P., and Clarkson, R. J.: Calculating and communicating ensemble-based volcanic ash dosage and concentration risk for aviation, Meteorol. Appl., 26, 253–266, https://doi.org/10.1002/met.1759, https://rmets.onlinelibrary.wiley.com/doi/abs/10.1002/met.1759, 2019.

Prata, F., Bluth, G., Rose, B., Schneider, D., and Tupper, A.: Comments on Failures in detecting volcanic ash from a satellite-based technique, Remote Sens. Environ., 78, 341–346, 2001.

Rieger, D., Bangert, M., Bischoff-Gauss, I., Förstner, J., Lundgren, K., Reinert, D., Schröter, J., Vogel, H., Zängl, G., Ruhnke, R., and Vogel, B.: ICON–ART 1.0 – a new online-coupled model system from the global to regional scale, Geosci. Model. Dev., 8, 1659–1676, https://doi.org/10.5194/gmd-8-1659-2015, https://www.geosci-model-dev.net/8/1659/2015/, 2015.

Rieger, L. A., Malinina, E. P., Rozanov, A. V., Burrows, J. P., Bourassa, A. E., and Degenstein, D. A.: A study of the approaches used to retrieve aerosol extinction, as applied to limb observations made by OSIRIS and SCIAMACHY, Atmos. Meas. Tech. Discussions, 2018, 1–21, https://doi.org/10.5194/amt-2017-446, https://www.atmos-meas-tech-discuss.net/amt-2017-446/, 2018.

Riemer, N., Vogel, H., Vogel, B., and Fiedler, F.: Modeling aerosols on the mesoscale-γ: Treatment of soot aerosol and its radiative effects, J. Geophys. Res.-Atmos., 108, https://doi.org/10.1029/2003jd003448, 2003.

Riemer, N., Ault, A. P., West, M., Craig, R. L., and Curtis, J. H.: Aerosol Mixing State: Measurements, Modeling, and Impacts, Rev. Geophys., 57, 187–249, https://doi.org/10.1029/2018RG000615, 2019.

Robock, A.: Volcanic eruptions and climate, Rev. Geophys., 38, 191–219, https://doi.org/10.1029/1998RG000054, 2000.

Rose, W. and Durant, A.: Fine ash content of explosive eruptions, J. Volcanol. Geoth. Res., 186, 32 – 39, https://doi.org/https://doi.org/10.1016/j.jvolgeores.2009.01.010, http://www.sciencedirect.com/science/article/pii/S037702730900016X, improved Prediction and Tracking of Volcanic Ash Clouds, 2009.

Schmidt, A., Witham, C. S., Theys, N., Richards, N. A. D., Thordarson, T., Szpek, K., Feng, W., Hort, M. C., Woolley, A. M., Jones, A. R., Redington, A. L., Johnson, B. T., Hayward, C. L., and Carslaw, K. S.: Assessing hazards to aviation from sulfur dioxide emitted by explosive Icelandic eruptions, J. Geophys. Res.-Atmos., 119, 14,180–14,196, https://doi.org/10.1002/2014jd022070, 2014.

Schröter, J., Rieger, D., Stassen, C., Vogel, H., Weimer, M., Werchner, S., Förstner, J., Prill, F., Reinert, D., Zängl, G., Giorgetta, M., Ruhnke, R., Vogel, B., and Braesicke, P.: ICON-ART 2.1: a flexible tracer framework and its application for composition studies in numerical weather forecasting and climate simulations, Geosci. Model. Dev., 11, 4043–4068, https://doi.org/10.5194/gmd-11-4043-2018, 2018.

Seinfeld, J. H. and Pandis, S. N.: Atmospheric Chemistry and Physics, Wiley John + Sons, 2016.

Sennet, S.: Global Volcanism Program, 2019, Report on Raikoke (Russia), Weekly Volcanic Activity Report, 26 June-2 July 2019, Tech. rep., Smithsonian Institution and US Geological Survey., 2019.

Shao, Y., Wyrwoll, K.-h., Chappell, A., Huang, J., Lin, Z., Mctainsh, G. H., Mikami, M., Tanaka, T. Y., Wang, X., and Yoon, S.: Dust cycle : An emerging core theme in Earth system science, Aeolian Res., 2, 181–204, https://doi.org/10.1016/j.aeolia.2011.02.001, 2011.

Tabazadeh, a. and Turco, R. P.: Stratospheric Chlorine Injection by Volcanic Eruptions: HCI Scavenging and Implications for Ozone., Science (New York, N.Y.), 260, 1082–6, https://doi.org/10.1126/science.260.5111.1082, http://www.ncbi.nlm.nih.gov/pubmed/17806335, 1993.

Textor, C., Graf, H.-F., Timmreck, C., and Robock, A.: Emissions from volcanoes, in: Emissions of Atmospheric Trace Compounds, edited by Granier, C., Artaxo, P., and Reeves, C. E., pp. 269–303, Springer Netherlands, Dordrecht, 2004.

Textor, C., Graf, H. F., Herzog, M., Oberhuber, J. M., Rose, W. I., and Ernst, G. G. J.: Volcanic particle aggregation in explosive eruption columns . Part II : Numerical experiments, J. Volcanol. Geoth. Res., 150, 378–394, https://doi.org/10.1016/j.jvolgeores.2005.09.008, 2006.

Theys, N., De Smedt, I., Yu, H., Danckaert, T., van Gent, J., Hörmann, C., Wagner, T., Hedelt, P., Bauer, H., Romahn, F., Pedergnana, M., Loyola, D., and Van Roozendael, M.: Sulfur dioxide retrievals from TROPOMI onboard Sentinel-5 Precursor: algorithm theoretical basis, Atmos. Meas. Tech., 10, 119–153, https://doi.org/10.5194/amt-10-119-2017, https://www.atmos-meas-tech.net/10/119/2017/, 2017.

Theys, N., Hedelt, P., De Smedt, I., Lerot, C., Yu, H., Vlietinck, J., Pedergnana, M., Arellano, S., Galle, B., Fernandez, D., Carlito, C., Barrington, C., Taisne, B., Delgado Granados, H., Loyola, D., and Van Roozendael, M.: Global monitoring of volcanic SO2 degassing with unprecedented resolution from TROPOMI onboard Sentinel-5 Precursor, Sci. Rep.-UK, 9, https://doi.org/10.1038/s41598-019-39279-y, 2019.

Timmreck, C.: Modeling the climatic effects of large explosive volcanic eruptions, Wires. Clim. Change, 3, 545–564, https://doi.org/10.1002/wcc.192, 2012.

Van Eaton, A. R., Mastin, L. G., Herzog, M., Schwaiger, H. F., Schneider, D. J., Wallace, K. L., and Clarke, A. B.: Hail formation triggers rapid ash aggregation in volcanic plumes, Nat. Commun., 6, 1–7, https://doi.org/10.1038/ncomms8860, http://dx.doi.org/10.1038/ncomms8860, 2015.

van Kempen, T. A., van Hees, R. M., Tol, P. J. J., Aben, I., and Hoogeveen, R. W. M.: In-flight calibration and monitoring of the Tropospheric Monitoring Instrument (TROPOMI) short-wave infrared (SWIR) module, Atmos. Meas. Tech., 12, 6827–6844, https://doi.org/10.5194/amt-12-6827-2019, https://www.atmos-meas-tech.net/12/6827/2019/, 2019.

Vernier, J.-P., Fairlie, T. D., Deshler, T., Natarajan, M., Knepp, T., Foster, K., Wienhold, F. G., Bedka, K. M., Thomason, L., and Trepte, C.: In situ and space-based observations of the Kelud volcanic plume: The persistence of ash in the lower stratosphere, J. Geophys. Res.-Atmos., 121, 11,104–11,118, https://doi.org/10.1002/2016JD025344, https://agupubs.onlinelibrary.wiley.com/doi/abs/10.1002/2016JD025344, 2016.

Vogel, A., Diplas, S., Durant, A. J., Azar, A. S., Sunding, M. F., Rose, W. I., Sytchkova, A., Bonadonna, C., Krüger, K., and Stohl, A.: Reference data set of volcanic ash physicochemical and optical properties, J. Geophys. Res.-Atmos., https://doi.org/10.1002/2016JD026328, 2017.

Vogel, B., Vogel, H., Bäumer, D., Bangert, M., Lundgren, K., Rinke, R., and Stanelle, T.: The comprehensive model system COSMO-ART – Radiative impact of aerosol on the state of the atmosphere on the regional scale, Atmos. Chem. Phys., 9, 8661–8680, https://doi.org/10.5194/acp-9-8661-2009, 2009.

von Savigny, C., Timmreck, C., Buehler, S., Burrows, J., Giorgetta, M., Hegerl, G., Horvath, A., Hoshyaripour, G. A., Hoose, C., Quaas, J., Malinina, E., Rozanov, A., Schmidt, H., Thomason, L., Toohey, M., and Vogel, B.: The Research Unit VolImpact: Revisiting the volcanic impact on atmosphere and climate ? preparations for the next big volcanic eruption, Meteorologische Zeitschrift, 29, 3–18, https://doi.org/10.1127/metz/2019/0999, http://dx.doi.org/10.1127/metz/2019/0999, 2020.

Walter, C.: Simulationen der Ausbreitung von Vulkanasche unter expliziter Beru¨cksichtigung der optischen Eigenschaften der Aschepartikel, Ph.D. thesis, Karlsruher Institut für Technologie (KIT), http://dx.doi.org/10.5445/KSP/1000095717{%}0A, 2019.

Weimer, M., Schröter, J., Eckstein, J., Deetz, K., Neumaier, M., Fischbeck, G., Hu, L., Millet, D. B., Rieger, D., Vogel, H., Vogel, B., Reddmann, T., Kirner, O., Ruhnke, R., and Braesicke, P.: An emission module for ICON-ART 2.0: implementation and simulations of acetone, Geosci. Model. Dev., 10, 2471–2494, https://doi.org/10.5194/gmd-10-2471-2017, 2017.

Weingartner, E., Burtscher, H., and Baltensperger, U.: Hygroscopic properties of carbon and diesel soot particles, Atmos. Environ., 31, 2311 – 2327, https://doi.org/https://doi.org/10.1016/S1352-2310(97)00023-X, http://www.sciencedirect.com/science/article/pii/S135223109700023X, 1997.

Wen, S. and Rose, W. I.: Retrieval of sizes and total masses of particles in volcanic clouds using AVHRR bands 4 and 5, J. Geophys. Res.-Atmos., 99, 5421–5431, 1994.

Wernli, H., Paulat, M., Hagen, M., and Frei, C.: SAL—A Novel Quality Measure for the Verification of Quantitative Precipitation Forecasts, Mon. Weather Rev., 136, 4470–4487, https://doi.org/10.1175/2008MWR2415.1, https://doi.org/10.1175/2008MWR2415.1, 2008.

Wernli, H., Hofmann, C., and Zimmer, M.: Spatial Forecast Verification Methods Intercomparison Project: Application of the SAL Technique, Weather Forecast., 24, 1472–1484, https://doi.org/10.1175/2009WAF2222271.1, https://doi.org/10.1175/2009WAF2222271.1, 2009.

Western, L. M., Watson, M. I., and Francis, P. N.: Uncertainty in two-channel infrared remote sensing retrievals of a well-characterised volcanic ash cloud, B. Volcanol., 77, 67, 2015.

Yu, P., Toon, O. B., Bardeen, C. G., Zhu, Y., Rosenlof, K. H., Portmann, R. W., Thornberry, T. D., Gao, R.-S., Davis, S. M., Wolf, E. T., de Gouw, J., Peterson, D. A., Fromm, M. D., and Robock, A.: Black carbon lofts wildfire smoke high into the stratosphere to form a persistent plume, Science, 365, 587–590, https://doi.org/10.1126/science.aax1748, https://science.sciencemag.org/content/365/6453/587, 2019.

Zängl, G., Reinert, D., Rípodas, P., and Baldauf, M.: The ICON (ICOsahedral Non-hydrostatic) modelling framework of DWD and MPI-M: Description of the non-hydrostatic dynamical core, Quart. J. Roy. Meteorol. Soc., 141, 563–579, https://doi.org/10.1002/qj.2378, 2015.